

Satellite quantification of methane emissions from South American countries: A high-resolution inversion of TROPOMI and GOSAT observations

Sarah E. Hancock¹, Daniel J. Jacob¹, Zichong Chen¹, Hannah Nesser², Aaron Davitt^{3,4}, Daniel J. Varon¹,
5 Melissa P. Sulprizio¹, Nicholas Balasus¹, Lucas A. Estrada¹, María Cazorla⁵, Laura Dawidowski⁶,
Sebastián Diez⁷, James D. East¹, Elise Penn¹, Cynthia A. Randles⁸, John Worden², Ilse Aben⁹, Robert J.
Parker^{10,11}, Joannes D. Maasakkers⁹

¹Harvard University, School of Engineering and Applied Sciences, Cambridge, MA, 02138, USA

10 ²Jet Propulsion Laboratory, California Institute of Technology, Pasadena, CA, 91011, USA

³WattTime, Oakland, CA, 94612, USA

⁴Climate TRACE, Denver, CO, 80022, USA

⁵Universidad San Francisco de Quito USFQ, Quito, 170901, Ecuador

⁶Gerencia Química, Comisión Nacional de Energía Atómica, San Martín, B1650KNA, Buenos Aires, Argentina

15 ⁷Centro de Investigación en Tecnologías para la Sociedad, Universidad del Desarrollo, Santiago, 7550000, Chile

⁸United Nations Environment Program International Methane Emissions Observatory, Paris, France

⁹SRON Netherlands Institute for Space Research, Leiden, the Netherlands

¹⁰National Centre for Earth Observation, University of Leicester, Leicester, UK

¹¹Earth Observation Science, School of Physics and Astronomy, University of Leicester, Leicester, UK

20

Correspondence to: Sarah E. Hancock (sarahhancock@g.harvard.edu)

Abstract. We use 2021 TROPOMI and GOSAT satellite observations of atmospheric methane in an analytical inversion to quantify national methane emissions from South America at up to 25 km × 25 km resolution. From the inversion, we derive optimal posterior estimates of methane emissions, adjusting a combination of national anthropogenic emission inventories reported by individual countries to the United Nations Framework Convention on Climate Change (UNFCCC), the UNFCCC-based Global Fuel Exploitation Inventory (GFEIv2), and the Emissions Database for Global Atmospheric Research (EDGARv7) as prior estimates. We also evaluate two alternative wetland emission inventories (WetCHARTs and LPJ-wsl) as prior estimates. Our best posterior estimates for wetland emissions are consistent with previous inventories for the Amazon but lower for the Pantanal and higher for the Paraná. Our best posterior estimate of South American anthropogenic emissions is 48 (41-56) Tg a⁻¹, where numbers in parentheses are the range from our inversion ensemble. This is 55% higher than our prior estimate and is dominated by livestock (65% of anthropogenic total). We find that TROPOMI and GOSAT observations can effectively optimize and separate national emissions by sector for 10 of the 13 countries and territories in the region, 7 of which account for 93% of continental anthropogenic emissions: Brazil (19 (16-23) Tg a⁻¹), Argentina (9.2 (7.9-11) Tg a⁻¹), Venezuela (7.0 (5.5-9.9) Tg a⁻¹), Colombia (5.0 (4.4-6.7) Tg a⁻¹), Peru (2.4 (1.6-3.9) Tg a⁻¹),

25
30

35 Bolivia (0.96 (0.66-1.2) Tg a⁻¹), and Paraguay (0.93 (0.88 – 1.0) Tg a⁻¹). Our estimates align with the prior estimates for
Brazil, Bolivia, and Paraguay, but are significantly higher for other countries. Emissions in all countries are dominated by
livestock (mainly enteric fermentation) except for oil/gas in Venezuela and landfills in Peru. Methane intensities from the
oil/gas industry are high in Venezuela (33%), Colombia (6.5%) and Argentina (5.9%). The livestock sector shows the largest
40 difference between our top-down estimate and the UNFCCC prior estimates, and even countries using complex bottom-up
methods report UNFCCC emissions significantly lower than our posterior estimate. These discrepancies could stem from
underestimations in IPCC-recommended bottom-up calculations or uncertainties in the inversion from aggregation error and
the prior spatial distribution of emissions.

1 Introduction

Methane (CH₄) is a potent greenhouse gas with a relatively short atmospheric lifetime of 9.1 ± 0.9 years (Szopa et al., 2021).
45 Methane atmospheric concentrations have nearly tripled since pre-industrial times, resulting in an emission-based radiative
forcing of 1.21 W m^{-2} compared to 2.16 W m^{-2} for CO₂ (Naik et al., 2021). Here we use satellite observations to quantify
and attribute methane emissions from South American countries, which have been estimated to contribute 14% of global
anthropogenic methane emissions (Worden et al., 2022) and are thought to be a major contributor to the methane rise over
the past decade (Y. Zhang et al., 2021).

50 The 194 Parties to the Paris Agreement, including all 12 South American countries, must regularly submit Nationally
Determined Contributions (NDCs) outlining their plans to reduce greenhouse gas emissions. These NDCs are based on
national emission inventories constructed using bottom-up methods that combine activity data for individual sectors with
emission factors, sometimes supplemented by direct measurements of individual sources. Bottom-up inventories tend to have
large uncertainties because emission factors (and sometimes the activity data) can be poorly quantified (Saunois et al., 2020),
55 and even direct emission measurements may not capture source variability. Atmospheric observations of methane
concentrations can offer additional top-down information to reduce these uncertainties through inverse analyses with an
atmospheric transport model, using the bottom-up inventories as prior estimates in the inversion (Jacob et al., 2022).

Anthropogenic emissions of methane come from many sectors, including oil/gas, coal, livestock, rice cultivation, landfills,
and wastewater treatment. Natural emissions are from wetlands, fires, termites, and geological seeps. In South America,
60 wetlands are a major natural methane source but again with large uncertainty (B. Zhang et al., 2017). South American
anthropogenic methane emissions are heavily dominated by livestock. Of particular importance is Brazil, which is estimated
to be the third-highest anthropogenic methane-emitting country globally (Worden et al., 2022) and has been identified as a
major contributor to the recent global rise in methane through livestock and wetland emissions (Y. Zhang et al., 2021, Qu et
al., 2024). Venezuela, Colombia, and Argentina also have high emissions (Worden et al., 2022).

65 Satellite observations in the shortwave infrared (SWIR) are particularly attractive for top-down emission estimates due to
their global coverage and sensitivity down to the surface. Inversions of data from the Greenhouse Gases Observing Satellite

(GOSAT, 2009-present) (Parker et al., 2020a) have been used to infer the distribution of methane emissions globally (Maasakkers et al., 2019; Janardanan et al., 2020; Qu et al., 2021) and regionally for South America (Tunnicliffe et al., 2020, Wilson et al., 2021). These inversions have identified significant discrepancies between top-down estimates and bottom-up
70 emissions inventories across South America. However, GOSAT observations are sparse, separated by about 250 km, which limits the spatial resolution that can be achieved, increasing uncertainties in attributing the top-down emissions to countries and sectors. The TROPospheric Monitoring Instrument (TROPOMI) (2018-present) provides global continuous daily mapping of atmospheric methane at $7 \text{ km} \times 5.5 \text{ km}$ nadir resolution (Lorente et al., 2023). This coverage in combination with high resolution provides TROPOMI with a unique capability for quantifying national emissions and attributing emissions to
75 sectors. This has recently been demonstrated for the United States (Nesser et al., 2024), the Middle East and North Africa (Chen et al., 2023), China (Chen et al., 2022, Liang et al., 2023), and Venezuela (Nathan et al., 2023).

Here we use TROPOMI observations in an inverse analysis of 2021 methane emissions over South America at up to 25 km resolution, using as prior estimates the national anthropogenic inventories reported to the United Nations Framework Convention on Climate Change (UNFCCC) under the Paris Agreement for the livestock, waste, and rice sectors. We use two
80 alternative bottom-up wetland emission inventories as prior estimates. We use a new TROPOMI satellite product that corrects surface, aerosol, and cloud artifacts with a machine learning algorithm trained by GOSAT data (Balasus et al., 2023). We also use GOSAT data, which though sparse provides unique information over wetlands. We quantify emissions by country and by sector and begin to identify causes for discrepancies between our estimates and those of the bottom-up inventories.

85 **2 Data and Methods**

We use methane observations from GOSAT and TROPOMI (Sect. 2.1) with the GEOS-Chem chemical transport model to optimize a state vector of mean methane emissions for 2021 over a rectilinear inversion domain covering South America (-57.5° to 13.25° latitude, -82.8125° to -33.75° longitude) at up to $0.25^\circ \times 0.3125^\circ$ resolution ($\sim 25 \text{ km} \times 25 \text{ km}$). We use a combination of countries' UNFCCC reports and global inventories as prior estimates of anthropogenic emissions in our
90 inversion (Sect. 2.2). We obtain posterior estimates of the state vector and the associated error covariance matrix through analytical solution for the minimum of the Bayesian cost function with lognormal prior errors (Sect. 2.3). We attribute inversion results to different methane emission sectors with the methodology described in Sect. 2.4. We conduct an ensemble of sensitivity inversions varying inversion parameters, including the choice of wetland prior estimate, to characterize related errors in the posterior estimate (Sect. 2.5).

95 **2.1 TROPOMI and GOSAT satellite observations**

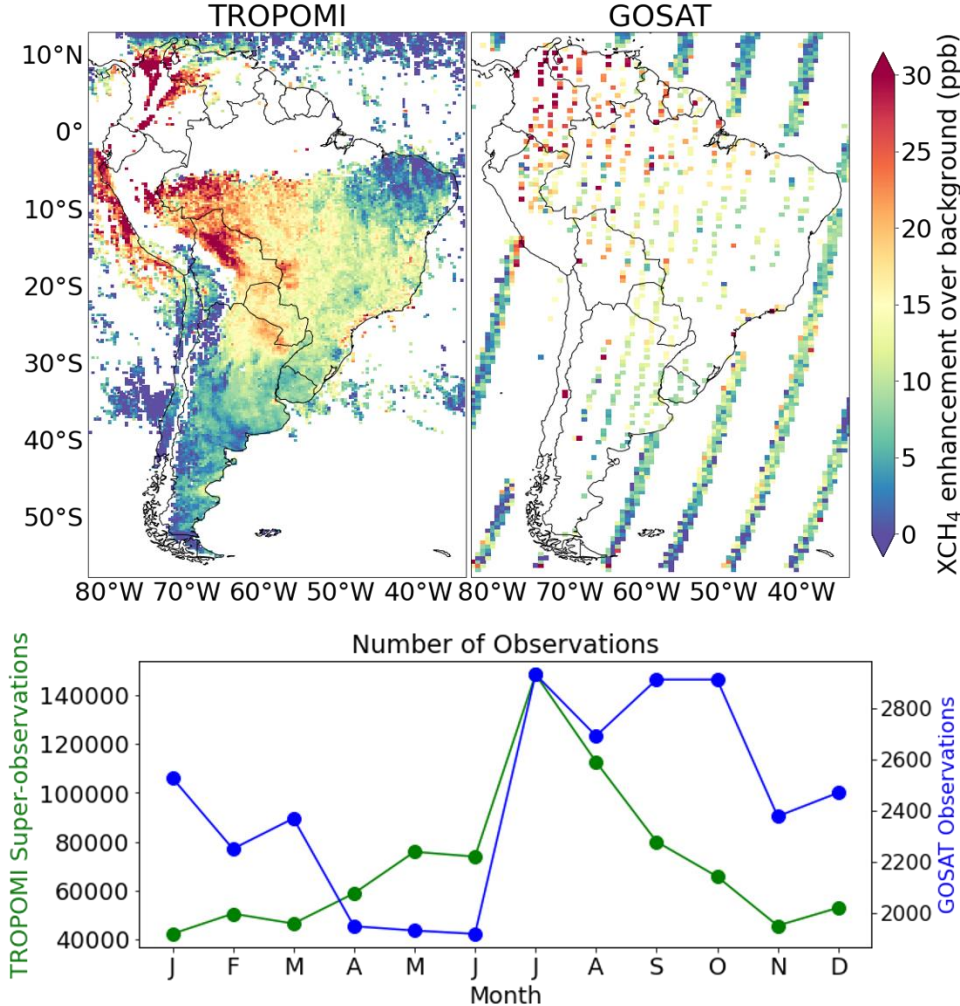
GOSAT, launched in 2009, has a 13:00 local overpass time and 10-km diameter pixels separated by about 250 km along-track and cross-track (Parker et al., 2020a). Dry column methane mixing ratios (XCH_4) are retrieved in the $1.65 \mu\text{m}$

absorption band with a CO₂ proxy method (Parker et al., 2011). The observations include a glint mode over the oceans. The CO₂ proxy method corrects for most surface and aerosol artifacts, yielding a global retrieval success rate of 23.5% (28.4% over South America) limited by cloud cover (Parker et al., 2020a). We use the GOSAT v9.0 proxy retrieval from Parker and Boesch (2020) which is available at <https://dx.doi.org/10.5285/18ef8247f52a4cb6a14013f8235cc1eb>. We remove GOSAT observations in mountainous areas defined by a standard deviation of surface altitude greater than 25 m within a pixel as reported in the GOSAT product. We also subtract 9.2 ppb from all GOSAT observations following Balasus et al. (2023) to remove the global mean bias versus ground-based methane column measurements from the Total Carbon Column Observing Network (TCCON). This subtraction is intended to enforce consistency with the blended TROPOMI product used as boundary conditions in the inversion. Although there are no TCCON observations in South America, the bias subtraction is of little importance because the boundary conditions are corrected anyway. This yields $m_{\text{GOSAT}} = 29,233$ observations for 2021 used in our inversion.

TROPOMI is on board the polar sun-synchronous Sentinel 5 Precursor satellite launched in 2017 with a 13:30 local overpass time, providing full global daily coverage with a spatial resolution of 7 km × 5.5 km in the nadir (Veefkind et al., 2012). It retrieves XCH₄ with a full-physics algorithm in the 2.3 μm absorption band in combination with the NIR (757 – 774 nm) band. Again, the observations include a glint mode over the oceans. The global success rate is 3% over land limited by dark or heterogeneous surfaces and cloud cover (Hasekamp et al., 2023). Mountainous scenes in South America have been previously found to be a challenge for TROPOMI ozone retrievals (Cazorla and Herrera, 2022) but the methane retrieval would be unsuccessful for such scenes in any case. It is well known that the TROPOMI XCH₄ data can be affected by retrieval artifacts correlated with SWIR surface albedo (Lorente et al., 2023). Here we use the TROPOMI product from Balasus et al. (2023), which uses a machine learning model to correct the TROPOMI v02.04.00 operational product of Lorente et al. (2023) by reference to the GOSAT v9.0 proxy retrieval. The blended product is available at <https://registry.opendata.aws/blended-tropomi-gosat-methane>. There are 7,264,168 successful TROPOMI retrievals over the inversion domain during 2021. We average them over GEOS-Chem 0.25°×0.3125° grid cells to produce 885,957 super-observations (Chen et al., 2023). We filter out TROPOMI observations in grid cells that have fewer than 30 individual TROPOMI retrievals in 2021. This yields $m_{\text{TROPOMI}} = 853,599$ super-observations for 2021 used in the inversion.

Figure 1 shows the resulting data for TROPOMI and GOSAT in 2021 as the mean XCH₄ enhancements after subtracting the time- and latitude-dependent background over the oceans used as boundary conditions in the inversion (Section 2.3). Subtracting the background is needed for visualization because of its 100 ppb latitudinal difference between the northern and southern tips of South America, but this subtraction is not applied in the inversion. We see significant XCH₄ enhancements over wetlands, livestock regions, and urban areas. There are few observations over the mountainous Andes, affecting much of Chile and Peru, so that the inversion for those countries relies significantly on glint observations offshore and on observations of transported methane. We also see that because of its use of the CO₂ proxy method, GOSAT is of particular value over the Amazon, where TROPOMI data are almost absent because of clouds and dark surfaces. GOSAT does not provide much additional coverage over the Andes because we filter out GOSAT observations over mountainous regions.

Satellite observations are distributed throughout the year but are densest during the southern hemisphere dry season (June-September) (Figure 1) due to a reduction of coverage over the Amazon in the wet season (Figure S1). We account for errors in the satellite retrievals ingested into the inversion as described in Section 2.3.



135

140

Figure 1: Atmospheric methane enhancements observed by TROPOMI and GOSAT over South America relative to the latitudinal background. The Figure shows the mean 2021 dry-column methane mixing ratios (XCH₄) after subtraction of time- and latitude-dependent background values over the oceans used as boundary conditions in the inversion. TROPOMI observations are on the native grid of the inversion (0.25°×0.3125°) and GOSAT points are shown on a 0.5°×0.625° grid for visibility. GOSAT samples repeatedly at the same locations, partly accounting for the apparent sparsity. Also shown in the lower panel is the distribution of GOSAT observations and TROPOMI super-observations over the course of the year.

2.2 Prior emissions

Fig. 2 shows the spatial distribution of prior emissions by sector on the $0.25^{\circ} \times 0.3125^{\circ}$ grid. Table 1 lists continental totals. Oil, gas, and coal emissions are from the Global Fuel Exploitation Inventory (GFEIv2) of Scarpelli et al. (2022), which uses detailed infrastructure data to spatially allocate emissions from countries' UNFCCC reports. Because GFEIv2 may not use emissions from countries' most recent reports, we list it separately from the other UNFCCC emissions which were obtained directly from countries' reports. National livestock, waste, and rice emissions are taken from each country's latest UNFCCC report (Table 2) and spatially distributed following the Emissions Database for Global Atmospheric Research (EDGARv7) inventory for 2021 (Crippa et al., 2022). Other minor anthropogenic emissions including industry, stationary combustion, mobile combustion, aircraft, composting, and field burning of agricultural residues are taken from EDGARv7. Anthropogenic emissions are assumed aseasonal except for rice, for which we use month-to-month variability from EDGARv6 (Crippa et al., 2021) (EDGARv7 does not provide monthly sectoral emission maps).

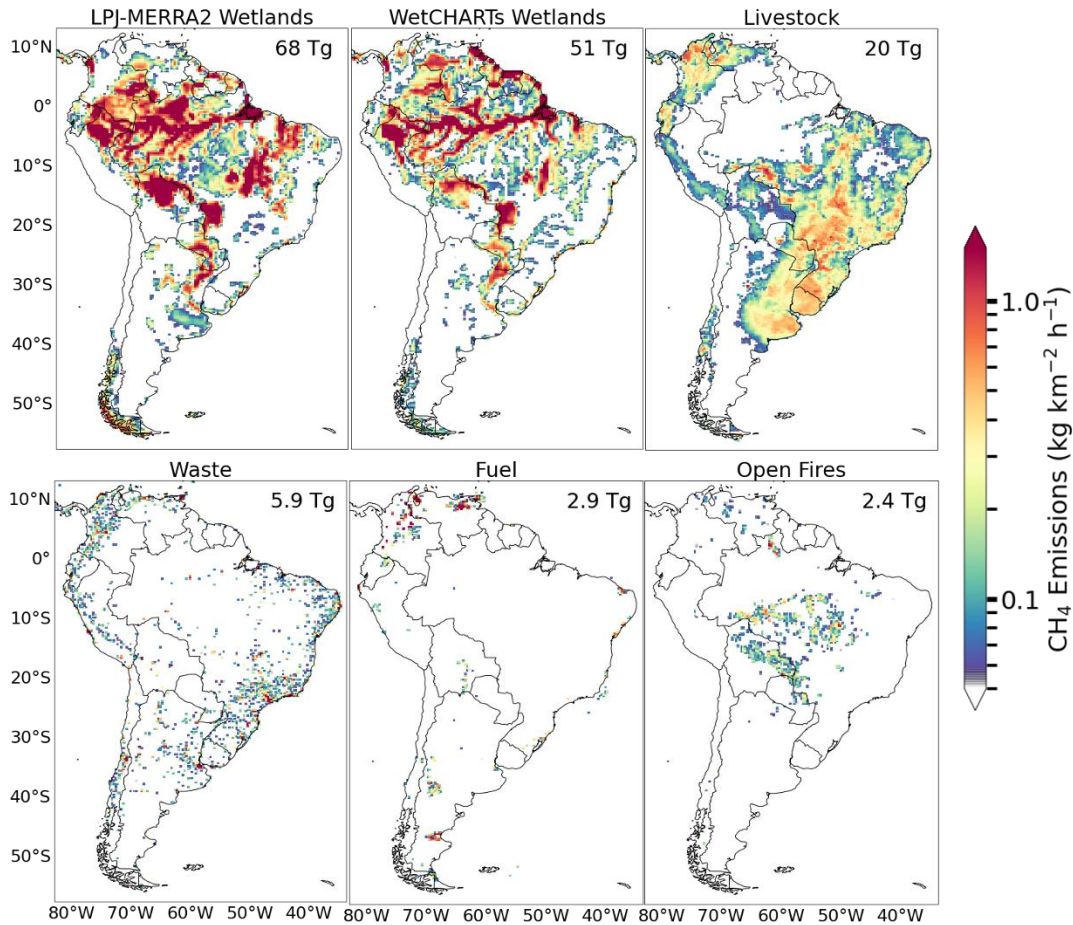
UNFCCC national totals for livestock, waste, and rice for Brazil, Guyana, Paraguay, and Uruguay are from the UNFCCC GHG Data Interface (https://di.unfccc.int/detailed_data_by_party, last accessed Jan 20, 2023). All other countries have produced more recent reports that are unavailable in the UNFCCC GHG Data Interface, so we inspect reports submitted by each country including National Communications (<https://unfccc.int/non-annex-I-NCs>, last accessed Jan 20, 2023) and Biennial Update Reports (<https://unfccc.int/BURs>, last accessed Jan 20, 2023), to obtain the most recent emissions estimates as detailed in Table S1. French Guiana is not independently reported and we use GFEIv2 for fuel and EDGARv7 for all other sectors.

Two alternative monthly wetland emission inventories for 2021 with $0.5^{\circ} \times 0.5^{\circ}$ spatial resolution are used as prior estimates: WetCHARTs and LPJ-wsl. WetCHARTs is an ensemble of parameterized inventories applying different inundation data, temperature dependence, and other factors (Bloom et al., 2017). We use the mean emissions from the nine high-performance members of the WetCHARTs v1.3.1 ensemble found by Ma et al. (2021) to best fit the results from a global GOSAT inversion and refer to it as WetCHARTs in what follows. LPJ-wsl is based on the Dynamic Global Vegetation model (Z. Zhang et al., 2016) driven here with NASA MERRA-2 meteorological data (Z. Zhang et al., 2018) and is henceforth referred to as LPJ-MERRA2. East et al. (2024) found that LPJ-MERRA2 could reproduce seasonal variations of atmospheric methane concentrations better than other wetland inventories, including WetCHARTS.

Other natural sources in our prior estimates include daily open-fire emissions for 2021 from the Global Fire Emissions Database version 4s (GFED4s) (van der Werf et al., 2017), termite emissions from Fung et al. (1991), and geological seepage emissions from Etiope et al. (2019) with global scaling to 2 Tg a^{-1} (Hmiel et al., 2020).

Figure 2 shows that South American emissions in the prior estimate are dominated by wetlands (62% of continental emissions averaged across LPJ-MERRA2 and WetCHARTs), mainly over the Amazon region but also extending into Paraguay (Pantanal) and Argentina (Paraná River basin). Livestock (22%), mainly enteric fermentation from cattle, is the largest anthropogenic source for almost all countries and is spatially distinct from wetlands. Landfills and wastewater

175 treatment, collectively referred to as waste (5.9%), follow population density and are large in all countries. Fossil fuel emissions are mostly from oil/gas (2.5%) and are concentrated in Venezuela and Argentina. Coal emissions are small (0.4%) and concentrated in Colombia. Rice emissions are also small (0.7%) and concentrated in southernmost Brazil. Open fires are a large seasonal source (2.5%) concentrated along the southern edge of the Amazon in Brazil and northern Bolivia.



180 **Figure 2: Bottom-up methane emission inventories used as prior estimates for the inversion. Panels show annual mean methane emissions for major sectors with continental totals inset. Wetland emissions for 2021 (inversion year) are shown for both WetCHARTs (mean of the nine members of the high-performing ensemble) and LPJ-MERRA2. Coal, oil, and gas emissions are from the GFEIv2 gridded version of the national inventories from individual countries reported to the UNFCCC. Other anthropogenic emissions are from countries' most recent UNFCCC reports with spatial allocation from EDGAR v7.**

185

190

195 **Table 1: Methane emissions in South America (Tg a⁻¹)**

| | Prior^a | Posterior^b |
|-------------------------------|--------------------------|------------------------------|
| Total | 96 | 121 (109-137) |
| Anthropogenic (UNFCCC) | 31 | 48 (41-56) |
| Livestock | 21 | 31 (27-37) |
| Waste^c | 5.7 | 7.8 (6.5-9.5) |
| Rice | 0.68 | 0.86 (0.74-1.4) |
| Oil/Gas | 2.4 | 6.2 (5.2-7.9) |
| Coal | 0.40 | 0.59 (0.42-1.4) |
| Other^d | 1.0 | 1.3 (1.1-1.5) |
| Natural | 56-74 | 74 (68-83) |
| Open Fires | 2.4 | 2.6 (2.4-3.0) |
| Wetlands | 52-68 ^e | 67 (62-75) |
| Seeps | 0.09 | 0.22 (0.17-0.30) |
| Termites | 2.6 | 3.8 (3.2-5.1) |

^a Prior emission estimates used in the inversion. Livestock, waste, and rice emissions are from national reports to the UNFCCC for years ranging from 2004 to 2020 (see Table S1 for individual countries). Oil/gas and coal are from GFEIv2 (Scarpelli et al., 2022). Wetland and open fire emissions are for 2021 (inversion year).

^b Median best estimates from the inversion of TROPOMI and GOSAT data for 2021, and ranges from the inversion ensemble.

200 ^c Including landfills and wastewater treatment

^d Including industry, stationary combustion, mobile combustion, aircraft, composting, and field burning of agricultural residues. Taken from EDGARv7.

^e Prior estimates for the inversion are taken either from the mean of the high-performing subset of the WetCHARTs ensemble (52 Tg a⁻¹) or from LPJ-MERRA2 (68 Tg a⁻¹).

205 **2.3 Analytical Inversion**

We use the Integrated Methane Inversion workflow (IMI 1.1) (Varon et al., 2022) with modifications as described below. The forward model for the inversion is the nested version of the GEOS-Chem 14.1.1 chemical transport model (<https://doi.org/10.5281/zenodo.4618180>), which relates methane emissions to atmospheric concentrations through atmospheric transport (Maasackers et al., 2019). GEOS-Chem is driven by meteorological fields from NASA GEOS-FP analyses at 0.25° × 0.3125° resolution. We use this native resolution in GEOS-Chem over South America and adjacent oceans (domain in Fig. 1) with dynamic boundary conditions outside the inversion domain updated every three hours from a

210

global archive of smoothed TROPOMI observations (Varon et al., 2022). That same archive is used as initial conditions, so that the simulation is initially unbiased relative to TROPOMI observations. The GEOS-Chem methane simulation includes chemical loss from oxidation by tropospheric OH with a corresponding methane lifetime of 10.8 years, consistent with the
 215 lifetime of 11.2 ± 1.3 years inferred from the methyl chloroform proxy (Prather et al., 2012). It also includes minor losses from oxidation by tropospheric Cl, oxidation in the stratosphere, and uptake by soils (Murguia-Flores et al., 2018). The lifetime of methane against all sinks is 9.1 ± 0.9 years (Szopa et al., 2021). We do not optimize these sinks here.

We select the state vector \mathbf{x} for the inversion with the Gaussian mixture model (GMM) of Turner and Jacob (2015) modified to include satellite observation density as a similarity criterion. The GMM selects emission patterns that the TROPOMI
 220 observations can effectively constrain, aiming to preserve native ($0.25^\circ \times 0.3125^\circ$) resolution for strong sources with high observation density while smoothing the solution in regions with low observation density or weak prior emissions. Similarity vectors defining proximity and commonality in sectoral emissions (as defined by the prior estimate) as well as the density of TROPOMI observations are used to construct Gaussian state vector elements. We use 600 Gaussian functions as state vector elements to balance aggregation and smoothing errors (Wecht et al., 2014), following the precedent of past regional
 225 inversions of similar domain size (Maasakkers et al., 2021, Chen et al., 2022, Chen et al., 2023). We also optimize boundary conditions for each quadrant (north, south, west, east) and for each season, for a total of $n = 616$ state vector elements.

We perform the inversion with lognormal error probability density functions (pdfs) for prior emissions. This prevents unphysical negative emissions and better captures the heavy tail of the emission distribution than a normal error assumption. Specifically, we optimize $\ln(\mathbf{x})$ instead of \mathbf{x} , such that the prior errors on $\ln(\mathbf{x})$ (henceforth denoted as \mathbf{x}') follow a normal
 230 distribution. We optimize the boundary condition elements of the state vector assuming normal error distributions.

The inversion finds the optimal estimate $\hat{\mathbf{x}}'$ of \mathbf{x}' assuming normal error distributions (lognormal in emission space) by minimizing the Bayesian cost function $J(\mathbf{x}')$ (Brasseur and Jacob, 2017):

$$J(\mathbf{x}') = (\mathbf{x}' - \mathbf{x}'_a)^T \mathbf{S}'_a^{-1} (\mathbf{x}' - \mathbf{x}'_a) + \gamma (\mathbf{y} - \mathbf{K}' \mathbf{x}')^T \mathbf{S}_o^{-1} (\mathbf{y} - \mathbf{K}' \mathbf{x}') , \quad (2)$$

where $\mathbf{x}' = \ln(\mathbf{x})$ and $\mathbf{x}'_a = \ln(\mathbf{x}_a)$, \mathbf{x}_a ($n \times 1$) is the prior emission estimate ($n = 616$), and \mathbf{y} ($m \times 1$) is the ensemble of
 235 TROPOMI super-observations and GOSAT observations. \mathbf{S}'_a ($n \times n$) is the prior error covariance matrix and \mathbf{S}_o ($m \times m$) is the observational error covariance matrix. We assume \mathbf{S}'_a and \mathbf{S}_o to be diagonal in absence of better objective information. $\mathbf{K}' \mathbf{x}' = \mathbf{K} \mathbf{x}$ is the GEOS-Chem forward model simulation of XCH₄ which is constructed from the GEOS-Chem vertical profiles of methane dry mixing ratios by applying TROPOMI or GOSAT averaging kernel vectors and prior vertical profiles. $\mathbf{K} = \frac{\partial \mathbf{y}}{\partial \mathbf{x}}$ ($m \times n$) is the Jacobian matrix that describes the linear sensitivity of \mathbf{y} to \mathbf{x} , and is constructed column by column by
 240 perturbing individual elements of \mathbf{x} in GEOS-Chem. $\mathbf{K}' = \frac{\partial \mathbf{y}}{\partial \mathbf{x}'}$ ($m \times n$) describes the sensitivity of \mathbf{y} to \mathbf{x}' , which is nonlinear but derived immediately from \mathbf{K} with matrix elements $k'_{i,j} = \frac{\partial y_i}{\partial \ln(x_j)} = x_j \frac{\partial y_i}{\partial x_j} = x_j k_{i,j}$ where i and j are indices of the observations and the state vector elements respectively. The regularization factor γ is used to prevent overfitting to observations caused by missing covariant structure (off-diagonal terms) in \mathbf{S}_o (Chevallier, 2007). Following the method of

Lu et al. (2021), we determine an optimal γ value such that $(\hat{\mathbf{x}}' - \mathbf{x}'_a)^T \mathbf{S}'_a^{-1} (\hat{\mathbf{x}}' - \mathbf{x}'_a) \approx n \pm \sqrt{2n}$, the expected value (± 1 standard deviation) of the Chi-square distribution with n degrees of freedom. This yields $\gamma = 0.05$ here.

We solve the nonlinear optimization problem iteratively using the Levenberg-Marquardt method (Rodgers, 2000):

$$\mathbf{x}'_{N+1} = \mathbf{x}'_N + (\gamma \mathbf{K}'_N{}^T \mathbf{S}'_o^{-1} \mathbf{K}'_N + (1 + \kappa) \mathbf{S}'_a^{-1})^{-1} (\gamma \mathbf{K}'_N{}^T \mathbf{S}'_o^{-1} (\mathbf{y} - \mathbf{K} \mathbf{x}'_N) - \mathbf{S}'_a^{-1} (\mathbf{x}'_N - \mathbf{x}'_a)), \quad (2)$$

where the coefficient κ is fixed at 10 following Chen et al. (2022), who found that using $\kappa = 10$ converges faster with no difference in results compared to other methods. N is the iteration number with $\mathbf{x}'_0 = \mathbf{x}'_a$, and \mathbf{K}'_N is evaluated for $\mathbf{x}' = \mathbf{x}'_N$.

We iterate on Eq. (2) until the differences of all state vector elements between two consecutive iterations (\mathbf{x}'_N and \mathbf{x}'_{N+1}) are smaller than 0.5% and then take $\hat{\mathbf{x}}' = \mathbf{x}'_{N+1}$ as the optimal posterior estimate. The posterior error covariance matrix $\hat{\mathbf{S}}'$ on the optimal posterior estimate is given by (Rodgers, 2000):

$$\hat{\mathbf{S}}' = (\gamma \mathbf{K}'^T \mathbf{S}'_o^{-1} \mathbf{K}' + \mathbf{S}'_a^{-1})^{-1}, \quad (3)$$

where $\mathbf{K}' = \mathbf{K}'_{N+1}$ is evaluated for the posterior estimate. The averaging kernel matrix \mathbf{A} defining the sensitivity of the solution to the true value is given by:

$$\mathbf{A} = \frac{\partial \hat{\mathbf{x}}'}{\partial \mathbf{x}'} = \mathbf{I}_n - \hat{\mathbf{S}}' \mathbf{S}'_a^{-1}, \quad (4)$$

where \mathbf{I}_n is the $n \times n$ identity matrix. The trace of \mathbf{A} , which is called the degrees of freedom for signal (DOFS), indicates the number of independent pieces of information on \mathbf{x}' obtained from the observations. We will refer to the averaging kernel sensitivity for individual state vector elements as the corresponding diagonal element of the averaging kernel matrix.

An implication of using lognormal error statistics for emissions is that the prior estimate \mathbf{x}_a is the median (not the mean) of a lognormal error pdf, and the inversion correspondingly optimizes the median of the lognormal emission pdf. But the UNFCCC national reports should be viewed as best prior estimates of the means of the emission pdfs since they are to be added across countries for the Global Stocktake. The median and the mean of a lognormal pdf are related by:

$$x_{\text{median}} = x_{\text{mean}} \exp\left[-\frac{s'}{2}\right], \quad (5)$$

where $s' = (\ln \sigma_g)^2$ is the error variance in normal space and σ_g is the geometric error standard deviation. Here we assume that the prior emissions are lognormally distributed with a geometric standard deviation of 2 ($\sigma_g = 2$), therefore $x_{\text{median}} = 0.79 x_{\text{mean}}$. We apply these corrections to the prior emission estimates from Section 2.2 for use in the inversion as \mathbf{x}_a , with the prior error covariance matrix \mathbf{S}'_a taken as a diagonal matrix of the error variances $s_a = (\ln 2)^2$.

The same operation in reverse is needed for interpreting the posterior emission estimates, which the inversion returns as the medians of the posterior lognormal error pdf with posterior error covariance matrix $\hat{\mathbf{S}}'$. From the posterior error variances \hat{s}'_j given by the diagonal elements of $\hat{\mathbf{S}}'$ for the individual state vector elements j , we apply for each element the conversion $\hat{x}_{j, \text{mean}} = \hat{x}_{j, \text{median}} \exp[\hat{s}'_j/2]$. The mean posterior estimates are therefore related to the mean prior estimates by:

$$\hat{x}_{j, \text{mean}} = \left(\frac{\hat{x}_j}{x_{j,a}}\right)_{\text{inversion}} \exp\left[\frac{\hat{s}'_j - s'_{j,a}}{2}\right] x_{j,a, \text{mean}}, \quad (6)$$

where $(\hat{x}_j/\hat{x}_{j,a})_{\text{inversion}}$ is the ratio of medians returned by the inversion. All results presented here are for the mean posterior
 275 estimates, which allows for the summing of inversion results geographically to obtain regional or national totals for
 comparison to the mean prior estimates. We set the prior error standard deviation on the boundary conditions to be 10 ppb,
 which is typical of the root mean square error (RMSE) of GEOS-Chem simulations using posterior emission estimates (Chen
 et al., 2022).

We use the residual error method (Heald et al., 2004) to estimate observational error variances including contributions from
 280 the TROPOMI and GOSAT instruments, the retrieval, and the forward model. This method takes the residual error between
 the observations and the forward model simulation with prior estimates (after removing the mean bias, to be corrected in the
 inversion) as measure of the observational error on the forward model grid. We do this separately for GOSAT and
 TROPOMI. The resulting mean observational error standard deviation for GOSAT is 11.2 ppb. To account for the error
 reduction resulting from averaging P individual TROPOMI retrievals into the super-observations y on the GEOS-Chem
 285 $0.25^\circ \times 0.3125^\circ$ grid, we employ the residual error method for super-observations developed by Chen et al. (2023). This
 method derives the observational error variance of the super-observations (σ_{super}^2) by separating the contributions in the
 individual observations from the transport error variance $\sigma_{\text{transport}}^2$ (perfectly correlated for the individual observations
 within a GEOS-Chem grid cell) and the satellite single-retrieval error variance ($\sigma_{\text{retrieval}}^2$):

$$\sigma_{\text{super}}^2 = \sigma_{\text{retrieval}}^2 \left(\frac{1-r_{\text{retrieval}}}{p} + r_{\text{retrieval}} \right) + \sigma_{\text{transport}}^2, \quad (7)$$

290 where $r_{\text{retrieval}}$ is the error correlation coefficient for the individual observations in a $0.25^\circ \times 0.3125^\circ$ grid cell averaged into a
 super-observation. Chen et al. (2023) obtained $\sigma_{\text{transport}} = 4.5$ ppb, $\sigma_{\text{retrieval}} = 16.5$ ppb, and $r_{\text{retrieval}} = 0.55$ for TROPOMI
 observations over the Middle East and North Africa. Our own fit of residual errors to Eq. (7) for South America yields
 $\sigma_{\text{transport}} = 4.3$ ppb, $\sigma_{\text{retrieval}} = 14.8$ ppb, and $r_{\text{retrieval}} = 0.21$. The average observational error standard deviation for the
 TROPOMI super-observations in the inversion domain is 7.9 ppb.

295 **2.4 Attributing posterior emissions to individual countries and sectors**

The posterior GMM state vector ($n \times 1$) can be mapped onto the p native $0.25^\circ \times 0.3125^\circ$ grid cells of the inversion domain
 using the GMM-generated weighting of each Gaussian on that grid as represented by a matrix \mathbf{W}_{GMM} ($p \times n$). The
 contributions from each of q emission sectors to the emissions in individual grid cells are taken from the prior inventories to
 produce a matrix $\mathbf{W}_{\text{sectors}}$ ($pq \times n$). We then apply a summation matrix \mathbf{W}_{agg} ($r \times pq$) to aggregate emissions over
 300 r countries or sectors of interest. The resulting matrix $\mathbf{W} = \mathbf{W}_{\text{agg}}\mathbf{W}_{\text{sectors}}$ ($r \times n$) represents the linear transformation from
 the posterior GMM state vector ($n \times 1$) to a reduced state vector ($r \times 1$) of sectoral or country-level emissions. The reduced
 state vector ($\hat{\mathbf{x}}_{\text{red}}$), posterior error covariance ($\hat{\mathbf{S}}_{\text{red}}$), and averaging kernel matrix (\mathbf{A}_{red}) are computed as:

$$\hat{\mathbf{x}}_{\text{red}} = \mathbf{W}\hat{\mathbf{x}}, \quad (8)$$

$$\hat{\mathbf{S}}_{\text{red}} = \mathbf{W}\hat{\mathbf{S}}\mathbf{W}^T, \quad (9)$$

305 $\mathbf{A}_{\text{red}} = \mathbf{WAW}^*$, (10)

where $\mathbf{W}^* = \mathbf{W}^T(\mathbf{W}\mathbf{W}^T)^{-1}$ is the Moore-Penrose pseudo-inverse of \mathbf{W} (Calisesi et al., 2005). We either aggregate together or make note of sectors that have an error correlation greater than 0.75 as given by $\hat{\mathbf{S}}_{\text{red}}$. The averaging kernel sensitivities for the aggregated emissions are the diagonal elements of \mathbf{A}_{red} and represent the ability of the inversion to quantify the emissions independently from the prior estimate (1 = fully, 0 = not at all).

310 This method assumes that the relative contributions of each sector to the total emissions in a given grid cell are correct, which introduces an additional source of uncertainty in the sectoral attribution of inversion results. Although the high resolution of our inversion reduces the impact of this assumption compared to coarser-resolution approaches, our ability to attribute posterior emissions to individual sectors is dependent on the spatial allocation of emissions in the prior inventories.

2.5 Inversion Ensemble

315 Our inversion described above makes assumptions on the values of inversion parameters including a geometric error standard deviation of the lognormal prior error distribution $\sigma_g = 2$, an error standard deviation $\sigma_b = 10$ ppb for boundary conditions, and a regularization factor $\gamma = 0.05$ where σ_g and σ_b are selected following Chen et al. (2023) and γ is determined as described in Section 2.3. The posterior error matrix of Eq. (3) represents the uncertainty in the analytical solution given this choice of inversion parameters, but it does not account for uncertainties in the parameters themselves,

320 including the prior emission estimate. The choice of wetland emission inventory used as prior estimate for the inversion could particularly affect results. To address this, we generate a 54-member ensemble of sensitivity inversions varying the parameters following Chen et al. (2023). The inversion ensemble includes (1) $\sigma_g = 1.5, 2, \text{ or } 2.5$, (2) $\sigma_b = 5, 10, \text{ or } 20$ ppb, (3) WetCHARTS or LPJ-MERRA2 wetland prior estimate, and (4) $\gamma = 0.025, 0.05, \text{ or } 0.1$. Because the uncertainty defined by the range of optimal estimates of this ensemble is larger than the posterior error from any single inversion, we report an

325 uncertainty in posterior estimates as the range of solutions given by the inversion ensemble. We consider this to be a conservative uncertainty estimate given that the ensemble covers a range of $\sigma_g, \sigma_b,$ and γ values comparable to past work (Chen et al., 2023, Nesser et al., 2024), we use the residual error method to account for errors in the observing system, and we additionally test two prior wetland inventories. However, this range does not account for uncertainty that can arise from parameters that are impossible to vary in the inversion without significant computational expense, such as the prior

330 distribution of emissions and the spatial aggregation in the state vector. Unless stated otherwise, we report the best posterior estimate of emissions as the median of this inversion ensemble (for each state vector element, prior emissions are scaled by the median posterior/prior emissions ratio across the ensemble).

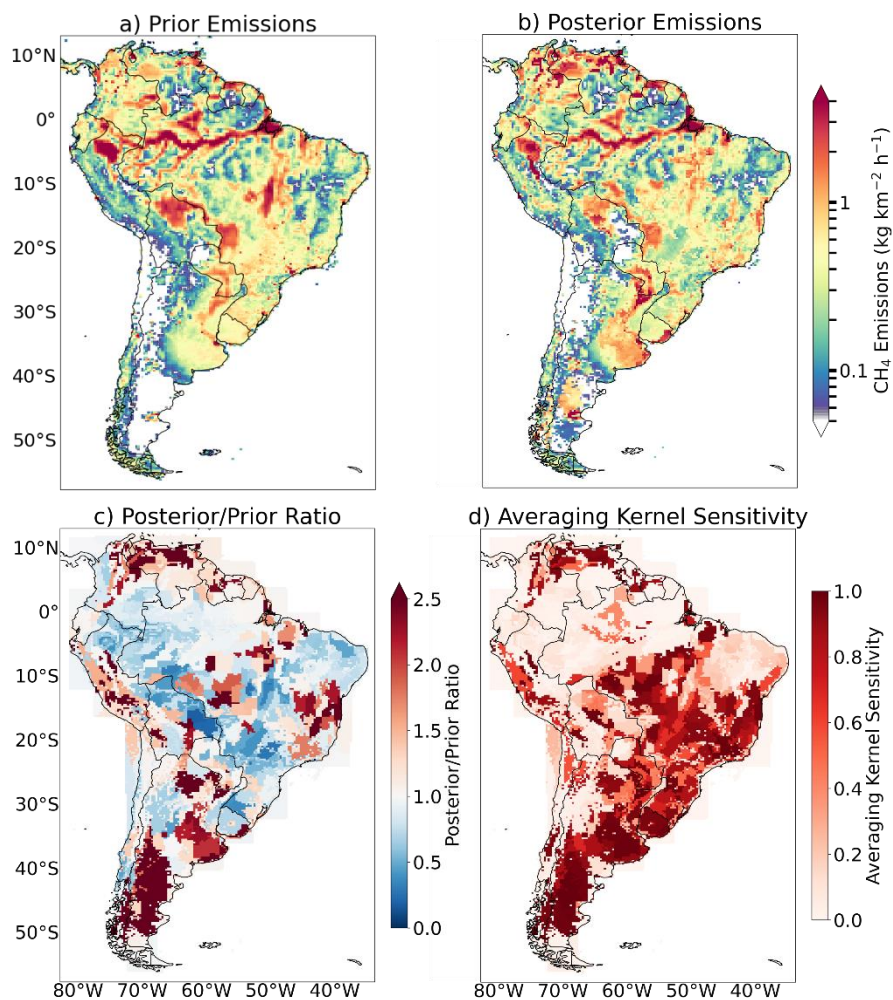
3 Results and Discussion

3.1 Continental-scale Results

335 Figure 3 shows the prior and posterior emission estimates over the continental scale for the median of the inversion ensemble, along with the median averaging kernel sensitivities. The median DOFS (sum of the averaging kernel sensitivities) are 144, out of a maximum of 616 defined by the state vector dimension. Low averaging kernel sensitivities over the Amazon and the Andes reflect the sparsity of observations.

The inversion effectively fits the emissions to the satellite data, as shown in Figure 4 where posterior emissions
340 decrease the mean GEOS-Chem model bias relative to the observations over the inversion domain from 3.04 to -0.03 ppb. The root-mean-square error (RMSE) decreases from 9.65 to 8.53 ppb, with improvement limited by the observational error (7.9 ppb for TROPOMI and 11.2 ppb for GOSAT). Figure S1 shows that this bias decreases in all seasons, but the extent of this decrease varies by both season and region; the remaining bias in the posterior is highest (2.34 ppb) in December through February when the observation count is lowest.

345 We also compare our results with in-situ data from the Amazon Tall Tower Observatory (ATTO) (Sierra et al., 2024), located in the center of the Amazon in northern Brazil. Figure 5 shows that the posterior emissions decrease the mean GEOS-Chem model bias relative to the ATTO measurements from -12.6 to 2.7 ppb, with a modest increase in correlation coefficient (0.75 to 0.79). While this bias reduction shows improvement in our posterior emissions, future work would greatly benefit from a higher density of in-situ measurements over South America. The Global Atmospheric Watch (GAW)
350 Programme provides in-situ data in Chile and Southern Argentina, but these sites are in low-emission areas where the sensitivity to satellite observations in the inversion is very small. The lack of validation with surface observations, not only of our inversion results but of the TROPOMI and GOSAT data itself over South America, should be considered when interpreting the results that follow.



355 **Figure 3: Optimization of methane emissions in South America on the $0.25^{\circ} \times 0.3125^{\circ}$ grid. Posterior emissions are our best estimates from the inversion of TROPOMI+GOSAT observations. Prior estimates are from UNFCCC reports (country totals for livestock, waste, rice), GFEIv2 (fuel), and EDGARv7 (other minor sources; spatial distribution for livestock, waste, and rice) for anthropogenic emissions and either LPJ-MERRA2 or WetCHARTs for wetland emissions (Figure 2: the average is shown here). The averaging kernel sensitivities indicate the ability of the observations to quantify emissions independently from the prior estimates on the $0.25^{\circ} \times 0.3125^{\circ}$ grid (1 = fully; 0 = not at all) as given by the diagonal elements of the averaging kernel matrix.**

360

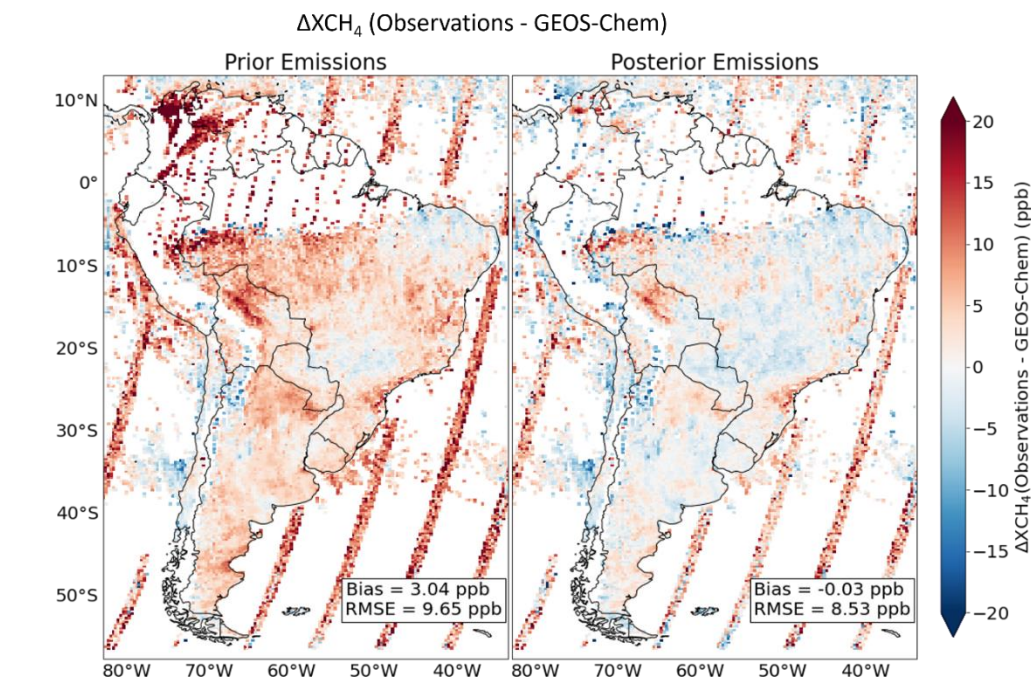


Figure 4: Differences between methane dry column mixing ratios (XCH_4) observed by TROPOMI+GOSAT and simulated by GEOS-Chem with prior emissions (including wetland emissions averaged across WetCHARTs and LPJ-MERRA2) and posterior emissions (median of the inversion ensemble). Legends give the mean bias and root-mean-square errors (RMSEs) for the prior and posterior.

365

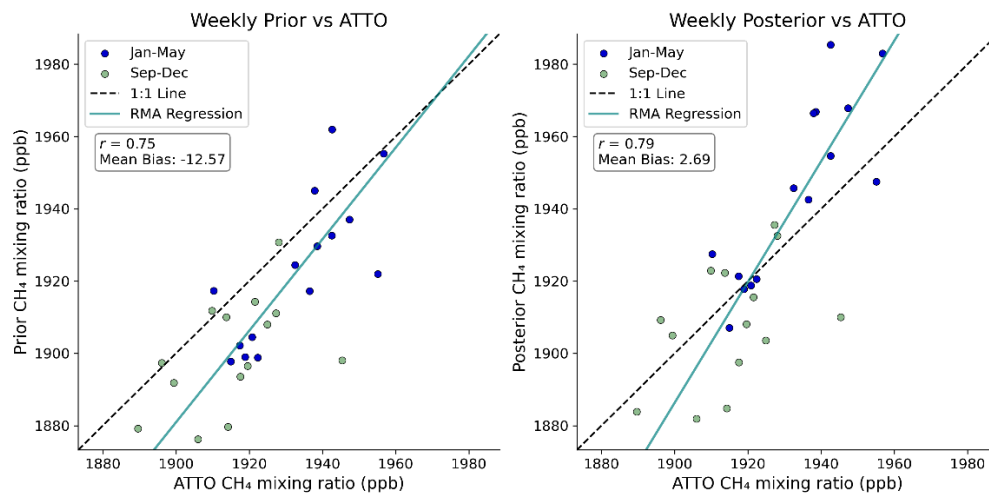


Figure 5: Evaluation of inversion results with independent in situ observations from the Amazon Tall Tower Observatory (ATTO; Sierra et al., 2024). The figure compares weekly average methane mixing ratios from GEOS-Chem simulations using prior or posterior emissions to weekly averages of ATTO measurements. Observations from January through May and September through December are taken from 79 m and 321 m altitude, respectively, and compared to the corresponding GEOS-Chem altitudes and times of day. Reduced-major-axis (RMA) linear regressions and the 1:1 line are also shown. The mean biases and correlation coefficients (r) are given inset. 4 outliers in the observations are not shown.

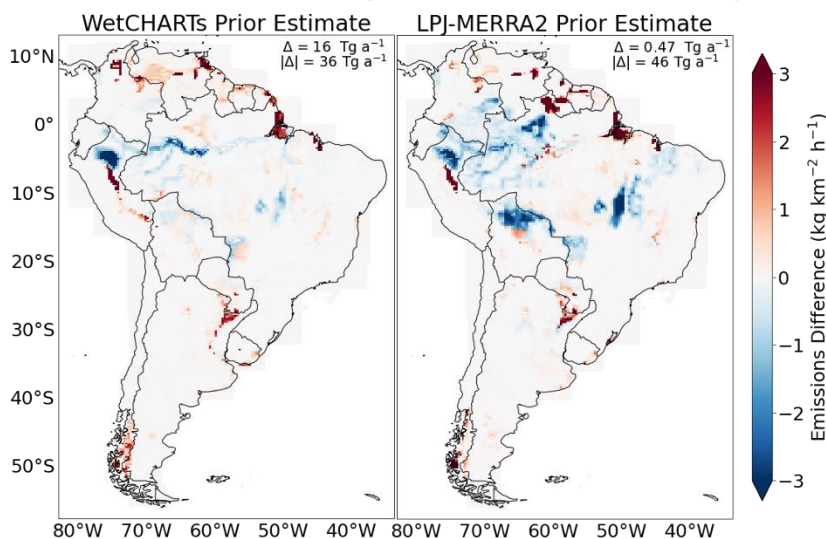
370

375 Table 1 compares total prior and posterior emission estimates for South America. Posterior emissions are 121 (109-137) Tg a⁻¹, where the parentheses indicate the range from the inversion ensemble. This represents a significant increase from the prior estimate of 96 Tg a⁻¹. Most of that increase is from anthropogenic emissions, which increase from 31 Tg a⁻¹ in the prior estimate to 48 (41-56) Tg a⁻¹. All sectors show emissions increases, with the largest for oil/gas (158%). On a regional scale, our estimate is comparable with those of Saunio et al. (2024) and Worden et al. (2022) for Brazil and Southwest South America, but larger in Northern South America (Figure S2). Further discussion of emissions by sector and country is presented below.

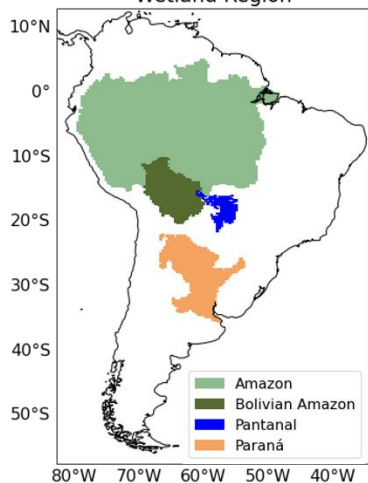
380 3.2 Wetland emissions

Figure 6 shows the difference between posterior and prior wetland emissions over South America from the WetCHARTs and LPJ-MERRA2 inversions with $\gamma=0.05$, $\sigma_g=2$, and $\sigma_b=10$ ppb. Inversion results are sensitive to the choice of prior estimate, even though the averaging kernel sensitivity is high, because of large differences in the prior spatial distributions (Figure 2). While the continental-scale adjustment to wetland emissions from the inversion is smaller for LPJ-MERRA2 (+0.5 Tg a⁻¹) than WetCHARTs (+15.9 Tg a⁻¹), the sum of the absolute value of spatial differences is larger for LPJ-MERRA2 (46 Tg a⁻¹) than WetCHARTs (36 Tg a⁻¹) (Figure 6). East et al. (2024) found that LPJ-MERRA2 better matched zonal mean atmospheric observations than WetCHARTs, but we find here that the WetCHARTs spatial distribution over South America better matches our posterior emissions estimate.

Δ Wetland Emissions (Posterior – Prior Estimates)



Wetland Region



| Region | Wetland Inventory | Wetland emissions (Tg a ⁻¹) | | Averaging Kernel Sensitivity |
|-----------------|-------------------|---|--------------------|------------------------------|
| | | Prior Estimate | Posterior Estimate | |
| Amazon | WetCHARTs | 32 | 32 (29-37) | 0.74 |
| | LPJ-MERRA2 | 46 | 39 (34-44) | 0.73 |
| Bolivian Amazon | WetCHARTs | 1.9 | 1.7 (1.6 - 2.0) | 0.60 |
| | LPJ-MERRA2 | 7.0 | 3.8 (3.6-4.4) | 0.63 |
| Pantanal | WetCHARTs | 1.8 | 1.6 (1.5 - 1.8) | 0.87 |
| | LPJ-MERRA2 | 2.0 | 1.3 (1.2-1.5) | 0.76 |
| Paraná | WetCHARTs | 0.87 | 2.0 (1.8 - 2.1) | 0.92 |
| | LPJ-MERRA2 | 1.4 | 2.1 (2.0 - 2.2) | 0.89 |
| South America | WetCHARTs | 52 | 67 (62 - 73) | 0.77 |
| | LPJ-MERRA2 | 68 | 69 (65 - 75) | 0.74 |

390

395

Figure 6: Adjustment to wetland emissions from inversion of TROPOMI and GOSAT data. The top panels show the differences between posterior and prior wetland emissions when either WetCHARTs or LPJ-MERRA2 wetland emissions are used as prior estimates. with $\gamma=0.05$, $\sigma_g=2$, and $\sigma_b=10$. The bottom panels show the prior and posterior wetland emissions for different regions. Ranges from the inversion ensembles are in parentheses. Boundaries of each region are defined using a combination of hydrological basin data from FAO's AQUASTAT (AQUASTAT database, available at <https://data.apps.fao.org/aquastat/?lang=en>, last accessed February 2024), and terrestrial ecoregions from the World Wildlife Fund (Olson et al., 2001).

Further examination of wetland emissions is shown in Figure 6 for four major regions: the Amazon Basin, the Bolivian Amazon, the Pantanal, and the Paraná. These regions constitute 68% and 83% of South American wetland emissions according to WetCHARTs and LPJ-MERRA2, respectively. We find emissions from the Amazon Basin of 32 (29-44) Tg a⁻¹, aligning with the WetCHARTs estimate and within the range of uncertainty of other estimates (31-56.5 Tg a⁻¹) (Wilson et

400

al., 2021; Wilson et al., 2016; Ringeval et al., 2014; Pangala et al., 2017; Basso et al., 2021). The Bolivian Amazon is a region of interest because of recent aircraft measurements showing methane emissions of 3.6 Tg a⁻¹ (France et al., 2022). Our best posterior estimate is 2.8 (1.6-4.4) Tg a⁻¹, again more consistent with WetCHARTs (1.9 Tg a⁻¹) than LPJ-MERRA2 (7 Tg a⁻¹).

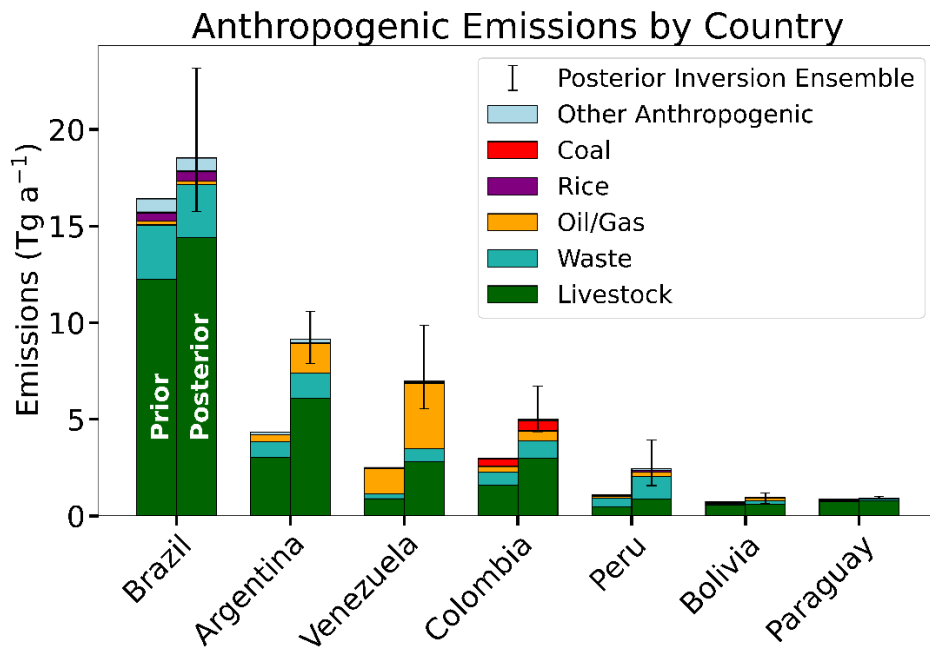
The Pantanal, located below the Amazon basin in Brazil, Bolivia, and Paraguay, is the largest seasonally flooded tropical grassland in the world. We estimate emissions from the Pantanal to be 1.5 (1.2-1.8) Tg a⁻¹ with downward adjustment from both LPJ-MERRA2 and WetCHARTs (1.8 and 2.0 Tg a⁻¹) and a lower estimate than the range of uncertainty of previous estimates (1.9 – 3.3 Tg a⁻¹) (Bastviken et al., 2010; Marani and Alvalá, 2007; Gloor et al., 2021).

The Paraná River wetland region extends from northern Argentina to the la Plata River Delta, which feeds into the Atlantic Ocean. We estimate emissions from this region to be 2.0 (1.8-2.2) Tg a⁻¹, a narrow range reflecting the high averaging kernel sensitivity. This is larger than WetCHARTs (0.87 Tg a⁻¹) and LPJ-MERRA2 (1.4 Tg a⁻¹). Parker et al. (2020b) found that WetCHARTs underestimated Paraná emissions in comparison to GOSAT due to wetland extent underestimation.

415 3.3 Anthropogenic emissions from individual countries and sectors

Figure 7 shows emissions by sector from the top seven anthropogenic emitting countries that make up 90% of posterior anthropogenic emissions over South America. Table 2 shows emissions for all countries. Posterior error correlations between countries are all less than 0.25, indicating the inversion's ability to effectively separate emissions between countries, but averaging kernel sensitivities are low (< 0.3) for Ecuador, French Guiana, and Suriname, because of a low density of observations and low prior emissions. Chile and Peru, despite lacking observations over the Andes, have moderately high averaging kernel sensitivities (0.61 and 0.46, respectively), indicating that the inversion is able to constrain emissions using glint observations offshore. We aggregate emissions from oil and gas as well as wastewater and landfills since posterior errors for these sectors are highly correlated. Posterior error correlations between other major sectors are generally low (< 0.25). Livestock has higher error correlations with rice (0.42) and biomass burning (0.44), but these are small sources.

425 We find that prior anthropogenic emissions for Brazil, Bolivia, and Paraguay are within the range of our inversion ensemble while Argentina, Venezuela, Colombia, and Peru have significantly higher top-down emissions. Livestock emissions in particular are much higher in all four of these countries. Argentina and Venezuela also have higher top-down oil/gas emissions than in the UNFCCC-based GFEIv2 prior estimate. Peru has a large contribution from waste emission that is underestimated in its UNFCCC report. Nathan et al. (2023) conducted a regional TROPOMI inversion over Venezuela and found total anthropogenic emissions in 2019 to be 3.6 (2.0-5.3) Tg a⁻¹. This is much lower than our estimate of 7.0 (5.5 – 9.9) mainly from differences in emissions from livestock (1.2 (0.9-1.6) Tg a⁻¹ vs our posterior 2.8 (2.0-4.5) Tg a⁻¹) and oil/gas (1.8 (0.9-2.7) Tg a⁻¹ vs 3.4 (3.1-5.5) Tg a⁻¹). Their lower estimate may be due to differences in the inversion setup, particularly their higher-resolution state vector over Northern Venezuela which could reduce the impact of aggregation error.



435 **Figure 7: National anthropogenic methane emissions from the top seven emitting countries in South America. Posterior estimates from inversion of 2021 TROPOMI and GOSAT observations are compared to countries' UNFCCC reports (livestock, waste, rice), GFEIv2 (coal, oil/gas), and EDGARv7 (other anthropogenic) which are taken as prior estimates for the inversion (Table 2). Waste includes emissions from landfills and wastewater treatment, which cannot be separated by the inversion. Vertical lines show the range of posterior estimates from our inversion ensemble.**

Table 2: National anthropogenic emissions (Tg a⁻¹) by country and sector^a

| Country | Total anthropogenic | Livestock | Waste | Rice | Oil/Gas | Coal | Other ^b | Averaging kernel sensitivity ^c |
|--------------------|---------------------|------------------|------------------|-------------------|-------------------|-------------------|--------------------|---|
| Argentina | | | | | | | | |
| Prior | 4.3 | 2.7 | 0.73 | 0.02 | 0.36 | <0.01 | 0.12 | |
| Posterior | 9.2 (7.9-11) | 6.1 (5.1-7.1) | 1.3 (1.1-1.6) | 0.02 (0.02-0.03) | 1.5 (1.4-1.6) | <0.01 | 0.21 (0.18-0.25) | 0.94 |
| Bolivia | | | | | | | | |
| Prior | 0.75 | 0.56 | 0.09 | 0.02 | 0.05 | <0.01 | 0.01 | |
| Posterior | 0.96 (0.66-1.2) | 0.61 (0.47-0.77) | 0.18 (0.11-0.20) | 0.02 (0.01-0.02) | 0.13 (0.07-0.19) | 0.18 (0.11-0.19) | 0.02 (0.01-0.02) | 0.6 |
| Brazil | | | | | | | | |
| Prior | 16 | 12.5 | 2.8 | 0.46 | 0.18 | 0.04 | 0.68 | |
| Posterior | 19 (16-23) | 14 (12-18) | 2.8 (2.4-3.3) | 0.49 (0.42-0.61) | 0.16 (0.13-0.17) | 0.04 (0.03-0.05) | 0.68 (0.58-0.84) | 0.75 |
| Chile | | | | | | | | |
| Prior | 0.67 | 0.23 | 0.29 | <0.01 | 0.04 | <0.01 | 0.04 | |
| Posterior | 0.88 (0.69-0.96) | 0.36 (0.26-0.41) | 0.41 (0.34-0.44) | 0.01 (<0.01-0.01) | 0.05 (0.04-0.15) | <0.01 | 0.05 (0.04-0.05) | 0.61 |
| Colombia | | | | | | | | |
| Prior | 3.0 | 1.6 | 0.69 | 0.03 | 0.28 | 0.35 | 0.05 | |
| Posterior | 5.0 (4.4-6.7) | 3.0 (2.5-4.2) | 0.91 (0.78-1.1) | 0.04 (0.03-0.05) | 0.48 (0.38-0.8) | 0.53 (0.35-1.4) | 0.08 (0.07-0.11) | 0.39 |
| Ecuador | | | | | | | | |
| Prior | 0.55 | 0.39 | 0.09 | 0.02 | 0.04 | <0.01 | 0.01 | |
| Posterior | 0.57 (0.55-0.70) | 0.4 (0.39-0.48) | 0.1 (0.1-0.12) | 0.02 (0.02-0.02) | 0.04 (0.03-0.07) | 0.04 (0.03-0.07) | 0.01 (0.01-0.02) | 0.16 |
| French Guiana | | | | | | | | |
| Prior ^d | <0.01 | <0.01 | <0.01 | <0.01 | <0.01 | <0.01 | <0.01 | |
| Posterior | <0.01 | <0.01 | <0.01 | <0.01 | <0.01 | <0.01 | <0.01 | 0.052 |
| Guyana | | | | | | | | |
| Prior | 0.05 | 0.02 | <0.01 | 0.02 | <0.01 | <0.01 | <0.01 | |
| Posterior | 0.07 (0.05-0.46) | 0.03 (0.02-0.13) | <0.01 | 0.03 (0.03-0.28) | <0.01 | <0.01 | <0.01 | 0.52 |
| Paraguay | | | | | | | | |
| Prior | 0.86 | 0.74 | 0.05 | 0.02 | <0.01 | <0.01 | 0.03 | |
| Posterior | 0.93 (0.88-1) | 0.80 (0.76-0.86) | 0.06 (0.05-0.07) | 0.03 (0.03-0.03) | <0.01 | <0.01 | 0.04 (0.03-0.04) | 0.83 |
| Peru | | | | | | | | |
| Prior | 1.1 | 0.46 | 0.44 | 0.05 | 0.09 | 0.01 | 0.04 | |
| Posterior | 2.4 (1.6-3.9) | 0.89 (0.64-1.5) | 1.1 (0.69-1.7) | 0.1 (0.07-0.19) | 0.22 (0.1-0.4) | 0.02 (0.01-0.03) | 0.07 (0.05-0.13) | 0.46 |
| Suriname | | | | | | | | |
| Prior | 0.03 | <0.01 | <0.01 | 0.01 | 0.01 | <0.01 | <0.01 | |
| Posterior | 0.03 (0.03-0.04) | <0.01 | <0.01 | 0.01 (0.01-0.01) | 0.01 (<0.01-0.01) | 0.01 (<0.01-0.01) | <0.01 | 0.28 |
| Uruguay | | | | | | | | |
| Prior | 0.77 | 0.69 | 0.05 | 0.01 | <0.01 | <0.01 | 0.01 | |
| Posterior | 1.1 (1.0-1.2) | 0.93 (0.8-1.0) | 0.14 (0.07-0.21) | 0.03 (0.03-0.03) | <0.01 | <0.01 | 0.02 (0.02-0.03) | 0.91 |
| Venezuela | | | | | | | | |
| Prior | 2.5 | 0.89 | 0.25 | 0.02 | 1.3 | <0.01 | 0.02 | |
| Posterior | 7.0 (5.5-9.9) | 2.8 (2.0-4.5) | 0.67 (0.45-1.2) | 0.06 (0.04-0.10) | 3.4 (3.1-5.5) | <0.01 | 0.06 (0.04-0.12) | 0.68 |

440

^a Prior estimates are from the latest country reports to the UNFCCC (see Table S1 for details) and the UNFCCC-based GFEIv2 inventory for fuel. Posterior results are from the inversion of TROPOMI and GOSAT data for 2021 and are shown as the median of the inversion ensemble, with ranges from the inversion ensemble in parentheses.

445 ^b Minor sources including industry, stationary combustion, mobile combustion, aircraft, composting, and field burning of agricultural residues. These minor sources are taken from EDGAR v7.

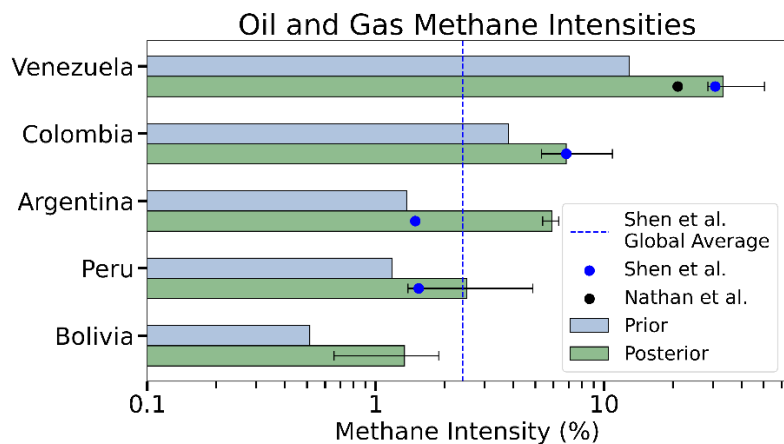
^c Ability of observations to quantify national anthropogenic emissions independently from the prior estimate (1 = fully, 0 = not at all) as measured by the diagonal terms of the averaging kernel matrix. Values are the median sensitivities across the inversion ensemble.

^d There is no UNFCCC report for French Guiana, and our prior estimate is taken from a combination of GFEI v2 and EDGAR v7 (see text).

450

Waste (landfills and wastewater) is a large emissions sector across South America that has a 50% higher top-down emissions estimate than the UNFCCC prior estimate. Countries estimate waste emissions using country-specific data on populations, waste generation rates, and landfill monitoring along with IPCC parameters for methane yield (IPCC, 2019). Our waste estimate for Brazil is consistent with its UNFCCC report but all other countries have higher estimates. Argentina (+59% in the top-down estimate relative to the prior estimate) and Peru (+150%) see the largest discrepancies. Despite significant efforts in Peru to improve their landfilling infrastructure, disposal of about 50% of the country's solid waste is still done improperly (Nueva ley y reglamento de residuos sólidos, 2024), much of which ends up in open dumpsites and could be unaccounted for in bottom-up estimates (Ziegler-Rodriguez et al., 2019). In Argentina, TROPOMI has been used previously to identify a strongly-emitting landfill in Buenos Aires (Maasackers et al., 2022), where we also find high posterior emissions.

Figure 8 compares the prior and posterior oil/gas methane intensity for each country defined as the total emissions from the oil/gas sector per unit of natural gas produced as methane (OGCI, 2022). We use national production data from EIA (EIA, 2023) and assume 90% of natural gas to be produced as methane as in Shen et al. (2023). We compare our posterior intensities to those inferred from Shen et al. (2023) for individual countries worldwide and from Nathan et al. (2023) for Venezuela in their inversions of TROPOMI data. Nathan et al. (2023) define methane intensity as the amount of methane emitted per unit of combined oil and gas production, rather than just gas production. We find that Venezuela, Peru, and Colombia have comparable posterior methane intensities to these previous studies, but Argentina's intensity is higher (5.9 (5.3-6.2) %) than the intensity inferred from Shen et al. (2023) (1.5%). The large difference between our posterior and prior estimates for Argentina may be due to our prior estimate from GFEIv2 not accounting for recent developments, particularly the substantial expansion of oil and gas extraction in the Neuquén basin in central-western Argentina over the past five years (Forni et al., 2021). All countries except Venezuela have methane intensities of magnitudes comparable to the global average of 2.4% inferred by Shen et al. (2023) from inversion of TROPOMI data and much higher than the industry target of 0.2% (OGCI, 2022), indicating a large potential to decrease emissions. Venezuela has the highest posterior methane intensity (33 (29-54) %) in South America, which can be explained by leakage from abandoned infrastructure as its oil production has declined (Nathan et al., 2023). Shen et al. (2023) found Venezuela to have the highest methane intensity of any country globally.



480 **Figure 8: Oil and gas methane intensities for major producing countries in South America. The methane intensity is defined as the**
amount of methane emitted per unit of methane gas produced for our posterior result and that of Shen et al (2023). Nathan et al.
(2023) define methane intensity as the amount of methane emitted per unit of combined oil and gas production, rather than just
gas production. Methane intensities computed from the prior and posterior emissions are compared to values inferred from Shen
et al. (2023) in a previous inversion of TROPOMI data for May 2018-February 2020 (they only report an upper emission estimate
of 1 Tg a⁻¹ for Bolivia) and from Nathan et al. (2023) in a TROPOMI inversion over Venezuela for 2019. Horizontal lines indicate
the ranges from our inversion ensemble. The vertical line shows the global mean methane intensity of 2.4% reported by Shen et al.
485 **(2023).**

3.4 Livestock emissions

Livestock accounts for over 65% of anthropogenic methane emissions in South America (Table 1), and over 90% of this
source is from enteric fermentation by cattle (FAOSTAT database, available at <https://www.fao.org/faostat/en/#data>, last
accessed February 2024). Bottom-up inventories estimate emissions from enteric fermentation by multiplying cattle
490 populations by an emission factor per head. The emission factor depends on age, size, feed, cattle type, and environment.
The IPCC (2019) gives different tiers of guidelines to incorporate this information into countries' bottom-up estimates. Tier
1 guidelines are to multiply cattle populations by emission factors that represent averages across all of Latin America. Tier 2
requires countries to calculate their own emission factors based on country-specific data on feed, size, productivity, and
amount of movement for different types of cattle. Tier 3 guidelines are not specific but could include the development of
495 sophisticated models considering diet composition or the fermentation process in more detail (Bannink et al., 2011).

Tier 1 emission factors for Latin America are calculated by the IPCC (2019) using data from 52 publications of which 32 are
for Brazil. These emission factors are 58 and 55 kg CH₄ head⁻¹ a⁻¹ for non-dairy cattle and 78 and 103 kg CH₄ head⁻¹ a⁻¹ for
dairy cattle in low and high productivity systems, respectively. Because these values are presented as averages across Latin
America, countries for which livestock is a dominant emission source are encouraged by IPCC (2019) to use Tier 2 or Tier 3
500 methods instead.

Many South American countries describe using a combination of Tier 2 and Tier 1 methods in their UNFCCC reports with
varying degrees of complexity. Argentina and Colombia, for example, both use complicated Tier 2 methods considering

livestock breed and temperature. Despite their complex bottom-up reporting, Argentina and Colombia see some of the largest discrepancies between their UNFCCC reports and our top-down estimate, indicating that the difference is not due to a lack of thoroughness in bottom-up calculations. The mismatch could be because IPCC Tier 2 methods can underestimate emission factors; Salas-Riega et al. (2022) showed that measured enteric emissions for both lactating and non-lactating cattle in the Peruvian high Andes were higher than those derived from IPCC Tier 2 methods (119 and 97 kg CH₄ head⁻¹ a⁻¹ for lactating and non-lactating cattle, respectively). It could also be because bottom-up methods are unable to capture the spatial and temporal variability of emission factors; Benaouda et al. (2020) reviewed daily measurements of cattle enteric fermentation in Latin America and found a wide range of emission factors, from 18 to 239 kg CH₄ head⁻¹ a⁻¹ with an average of 68 kg CH₄ head⁻¹ a⁻¹.

One possible weakness in our inversion is the reliance on EDGAR v7 for the prior spatial distribution of livestock emissions on the 0.25°×0.3125° grid. EDGAR spatially allocates emissions by using an array of proxy datasets including animal density and global land cover data (Crippa et al., 2024). Errors in this spatial distribution would propagate to inversion results by affecting both the optimal solution to the inverse problem (Yu et al., 2022) and the attribution of 0.25°×0.3125° posterior emissions to specific sectors (Shen et al., 2021). Figure 9 shows 2021 emissions from 779 individual feedlots and dairies in Northern Argentina and Southern Brazil estimated by Climate TRACE by using artificial intelligence to identify facility locations in PlanetScope (Planet Team, 2021) satellite imagery, assuming livestock numbers to be proportional to facility area, and applying 2006 IPCC emission factors (Davitt et al., 2023). The high emissions in northern Argentina do not match the spatial distribution from EDGAR (Figure 2). The right panel of Figure 9 compares our prior and posterior emission estimates to the Climate TRACE values for inversion grid cells dominated by livestock. Our values are higher because Climate TRACE estimates are limited to larger feedlots visible in PlanetScope imagery. However, we find better spatial correlations between Climate TRACE and our posterior emissions ($r = 0.44$, $p = 0.0004$) than our prior emissions ($r = -0.11$, $p = .42$). The Climate TRACE database could be useful as prior estimate for future inversions but would need to be more comprehensive. Another possible source of error is the overlap between livestock activities and agricultural burning, particularly in Argentina (Puliafito et al., 2020). Small fires, often set to clear waste and prepare fields for planting, may be too small to be captured accurately in the prior inventories (Randerson et al., 2012).

Future inversions could be improved by using country-specific, spatially-distributed emissions inventories as prior estimates when available. Argentina, for example, offers a spatially-gridded agriculture-specific emissions inventory in which livestock emissions are much more concentrated than in EDGAR (Puliafito et al., 2020), which may not have as precise, country-specific data to spatially allocate emissions. Using national, gridded inventories as prior estimates when available would not only reduce a major source of uncertainty in the inversion but would also make top-down results more policy-relevant.

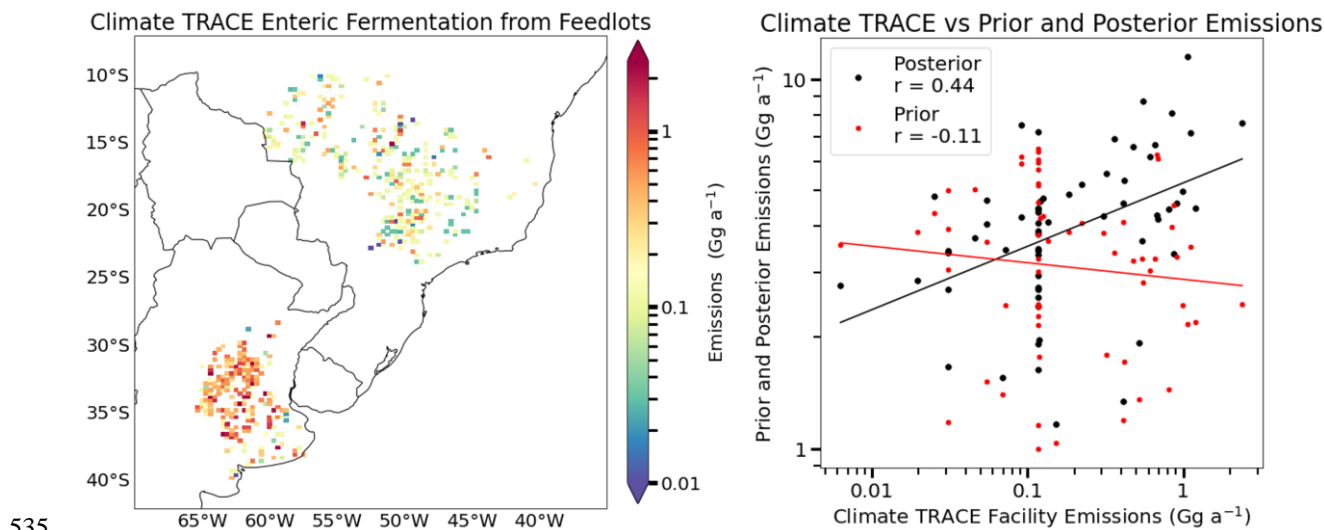


Figure 9: Satellite-informed spatial distribution of enteric fermentation emissions from feedlots and dairies in southern Brazil and northern Argentina from Climate TRACE (Davitt et al., 2023). The left panel shows the distribution of emissions from individual feedlots averaged onto the native $0.25^{\circ} \times 0.3125^{\circ}$ grid cells of our inversion. The right panel compares our prior and posterior emissions to the Climate TRACE data for grid cells where the inversion has averaging kernel sensitivities greater than 0.5, fewer than 50 grid cells aggregated within the state vector element, and more than 50% of prior emissions are from livestock. Reduced-major-axis linear regressions are also shown.

4 Conclusions

We used 2021 TROPOMI and GOSAT satellite observations of atmospheric methane (XCH_4) in a high-resolution analytical inversion to infer methane emissions from South America at up to $25 \text{ km} \times 25 \text{ km}$ resolution. The goal of this work was to use the national inventories submitted to the United Nations Framework Convention on Climate Change (UNFCCC) under the Paris Agreement in tandem with satellite methane observations to begin to identify reasons for the mismatch between top-down and bottom-up estimates over South America.

545

We used national emissions inventories reported by individual countries to the UNFCCC, gridded using EDGARv7, as the prior estimate for livestock, waste, and rice in the inversion; for fossil fuel sources, we used GFEIv2 as the prior estimate. For wetlands we used two alternative prior estimates, from WetCHARTs and LPJ-MERRA2, with different spatial distributions. We obtained best posterior estimates of emissions analytically through Bayesian synthesis of these prior estimates with the information from the TROPOMI and GOSAT observations. We used a blended TROPOMI+GOSAT product that corrects spatially variable biases and artifacts in the TROPOMI data using information from GOSAT. Although TROPOMI data is in general much denser than GOSAT, GOSAT provides unique coverage over the Amazon where TROPOMI data is sparse. The inversion used variable resolution with a Gaussian mixture model (GMM) state vector that enforces native 25-km resolution in source regions with high observation density. Analytical solution to the inversion enabled the creation of an inversion ensemble with 54 members for conservative uncertainty estimates on posterior emissions.

550

555

Total posterior emissions for South America are 121 (109-137) Tg a⁻¹, where the best estimate is the median of our inversion ensemble, and the range is in parentheses. This is significantly higher than the prior estimate of 96 Tg a⁻¹. Most of the increase is from anthropogenic emissions, which increase from 31 Tg a⁻¹ in the prior estimate to 48 (41-56) Tg a⁻¹. Anthropogenic emissions are dominated by livestock (65%), followed by waste (16%), and oil/gas (13%). Total anthropogenic emissions in South America are 55% higher than in the prior estimate, reflecting increases in emissions from oil/gas (+158%), livestock (+48%), and waste (+37%).

We obtain best posterior estimates of wetland emissions from the Amazon (32 (29-44) Tg a⁻¹), the Bolivian Amazon (2.8 (1.6-4.4) Tg a⁻¹), the Pantanal (1.5 (1.2-1.8) Tg a⁻¹), and the Paraná (2.0 (1.8-2.2) Tg a⁻¹). Our estimate for the Amazon is consistent with past estimates, but our estimate for the Pantanal is lower. Emissions from the Paraná are much higher than in either WetCHARTS or LPJ-MERRA2. Posterior wetland continental total emissions agree better with LPJ-MERRA2 than WetCHARTs, but the posterior spatial distribution better matches WetCHARTs.

We compare the bottom-up estimates of anthropogenic emissions from individual countries to our best sector-resolved posterior estimates. We find that TROPOMI and GOSAT observations can effectively resolve emissions from individual countries except Ecuador and Suriname. The top seven emitting countries including Brazil, Argentina, Venezuela, Colombia, Peru, Bolivia, and Paraguay make up 93% of the total anthropogenic emissions in the region, with Brazil contributing the highest amount (40%). All countries except Bolivia, Brazil, and Suriname show larger top-down anthropogenic emissions estimates than the prior estimate. Waste emissions are higher in the posterior estimate than the prior estimate, particularly in Peru. Oil/gas emissions are also higher in the posterior in all producing countries except Brazil. We find high methane intensities from the oil/gas sector in Venezuela (33 (29-54) %), Colombia (6.5 (5.1-10.8) %), and Argentina (5.9 (5.3-6.2) %).

We examine livestock emissions and their reporting to UNFCCC in more detail. These emissions are over 90% from enteric fermentation by cattle. We find that even countries with complex Tier 2 reporting methods report livestock emissions much lower than our posterior estimate. These differences may stem from underestimations in IPCC Tier 2 methods or the inability of bottom-up approaches to capture spatial and temporal variability in emission factors. They may also be the result of uncertainty in the inversion arising from aggregation error or the prior spatial distribution of livestock emissions.

South America is a heterogeneous continent with a complex range of drivers of emissions and methodologies used to calculate them. Future work would benefit from partnership with local experts to make stronger connections between top-down estimates and bottom-up data in specific countries. Top-down estimates can provide additional information to improve our understanding of methane emissions, but attribution to sectors is dependent on the choice of prior distribution of emissions; country-specific information can improve this prior estimate and thus the inversion results. Further, satellite observations of methane are validated by in-situ data primarily from the Northern Hemisphere. The credibility of future inversion results over South America would be greatly enhanced by comprehensive and systematic in-situ methane observations across the region.

5 Data Availability

The blended TROPOMI+GOSAT satellite observations version 2 are available at <https://registry.opendata.aws/blended-tropomi-gosat-methane> (Balasus et al., 2023). The GOSAT methane retrievals version 9.0 are available at <https://doi.org/10.5285/18ef8247f52a4cb6a14013f8235cc1eb> (Parker and Boesch, 2020). Oil, gas, and coal emissions from the GFEIv2 inventory are available at <https://doi.org/10.7910/DVN/HH4EUM> (Scarpelli and Jacob, 2021). Methane emissions by sector from EDGARv7 are available at https://edgar.jrc.ec.europa.eu/dataset_ghg70 (Crippa et al., 2022). Wetland emissions from WetCHARTs v1.3.1 are available at <https://doi.org/10.3334/ORNLDAAAC/1915> (Ma et al., 2021).

6 Author contributions

600 SH and DJJ contributed to the study conceptualization. SH conducted the data and modeling analysis with contributions from DJJ, ZC, HN, AD, DJV, MPS, NB, LAE, JDE, EP, CAR, JW, IA, RJP, and JDM. SH and DJJ wrote the paper with input from all authors. During the revision process, MC, LD, and SD were added as co-authors to strengthen the analysis, improve the clarity of the manuscript, and confirm the totals obtained from UNFCCC reports.

7 Competing Interests

605 At least one of the co-authors is a member of the editorial board of Atmospheric Chemistry and Physics.

8 Acknowledgements

This work was supported by the Harvard University Climate Change Solutions Fund (CCSF), by the NASA Carbon Monitoring System (CMS), and by a National Science Foundation Graduate Research Fellowship under grant no. DGE 2140743. This research has also been funded in the framework of UNEP's International Methane Emissions Observatory (IMEO). Part of this research was carried out at the Jet Propulsion Laboratory, California Institute of Technology, under a contract with the National Aeronautics and Space Administration supported by NASA ROSES Grant 18-CMS18-0018. This research was also supported in part by an appointment to the NASA Postdoctoral Program at the Jet Propulsion Laboratory, California Institute of Technology, administered by Oak Ridge Associated Universities under contract with NASA. RJP is funded via the UK National Centre for Earth Observation (Grant: NE/W004895/1). The GOSAT data generation was supported by the Natural Environment Research Council (NERC grant reference number NE/X019071/1, "UK EO Climate Information Service"). We also acknowledge funding from the ESA GHG-CCI and Copernicus C3S projects (grant no. C3S2_312a_Lot2). This research used the ALICE high-performance computing facility at the University of Leicester for the GOSAT retrievals. We thank the Japanese Aerospace Exploration Agency, National Institute for Environmental Studies and the Ministry of Environment for the GOSAT data and their continuous support as part of the Joint Research Agreement. We

620 thank Carlos Sierra for useful discussions regarding the use of ATTO data. We also thank the Instituto Nacional de Pesquisas da Amazonia (INPA) and the Max Planck Society for continuous support. We acknowledge the support by the German Federal Ministry of Education and Research (BMBF contracts 01LB1001A and 01LK1602B) and the Brazilian Ministério da Ciência, Tecnologia e Inovação (MCTI/FINEP contract 01.11.01248.00) as well as the Amazon State University (UEA), FAPEAM, LBA/INPA and SDS/CEUC/RDS-Uatumã.

625 **References**

- Nueva ley y reglamento de residuos sólidos: <https://www.minam.gob.pe/gestion-de-residuos-solidos/nueva-ley-de-residuos-solidos/>, last access: 16 September 2024.
- Balagus, N., Jacob, D. J., Lorente, A., Maasackers, J. D., Parker, R. J., Boesch, H., Chen, Z., Kelp, M. M., Nesser, H., and Varon, D. J.: A blended TROPOMI+GOSAT satellite data product for atmospheric methane using machine learning to correct retrieval biases, *Atmospheric Measurement Techniques*, 16, 3787–3807, <https://doi.org/10.5194/amt-16-3787-2023>, 2023.
- Bannink, A., van Schijndel, M. W., and Dijkstra, J.: A model of enteric fermentation in dairy cows to estimate methane emission for the Dutch National Inventory Report using the IPCC Tier 3 approach, *Animal Feed Science and Technology*, 166–167, 603–618, <https://doi.org/10.1016/j.anifeedsci.2011.04.043>, 2011.
- 635 Basso, L. S., Marani, L., Gatti, L. V., Miller, J. B., Gloor, M., Melack, J., Cassol, H. L. G., Tejada, G., Domingues, L. G., Arai, E., Sanchez, A. H., Corrêa, S. M., Anderson, L., Aragão, L. E. O. C., Correia, C. S. C., Crispim, S. P., and Neves, R. A. L.: Amazon methane budget derived from multi-year airborne observations highlights regional variations in emissions, *Commun Earth Environ*, 2, 1–13, <https://doi.org/10.1038/s43247-021-00314-4>, 2021.
- 640 Bastviken, D., Santoro, A. L., Marotta, H., Pinho, L. Q., Calheiros, D. F., Crill, P., and Enrich-Prast, A.: Methane Emissions from Pantanal, South America, during the Low Water Season: Toward More Comprehensive Sampling, *Environ. Sci. Technol.*, 44, 5450–5455, <https://doi.org/10.1021/es1005048>, 2010.
- Brasseur, G. P. and Jacob, D. J.: *Modeling of Atmospheric Chemistry*, Cambridge University Press, Cambridge, <https://doi.org/10.1017/9781316544754>, 2017.
- 645 Calisesi, Y., Soebijanta, V. T., and van Oss, R.: Regridding of remote soundings: Formulation and application to ozone profile comparison, *Journal of Geophysical Research: Atmospheres*, 110, <https://doi.org/10.1029/2005JD006122>, 2005.
- Cazorla, M. and Herrera, E.: An ozonesonde evaluation of spaceborne observations in the Andean tropics, *Sci Rep*, 12, 15942, <https://doi.org/10.1038/s41598-022-20303-7>, 2022.
- 650 Chen, Z., Jacob, D., Nesser, H., Sulprizio, M., Lorente, A., Varon, D., Lu, X., Shen, L., Qu, Z., Penn, E., and Yu, X.: Methane emissions from China: a high-resolution inversion of TROPOMI satellite observations, *Atmospheric Chemistry and Physics Discussions*, 1–31, <https://doi.org/10.5194/acp-2022-303>, 2022.

- 655 Chen, Z., Jacob, D. J., Gautam, R., Omara, M., Stavins, R. N., Stowe, R. C., Nesser, H. O., Sulprizio, M. P., Lorente, A., Varon, D. J., Lu, X., Shen, L., Qu, Z., Pendergrass, D. C., and Hancock, S.: Satellite quantification of methane emissions and oil/gas methane intensities from individual countries in the Middle East and North Africa: implications for climate action, *EGUsphere*, 1–42, <https://doi.org/10.5194/egusphere-2022-1504>, 2023.
- Chevallier, F.: Impact of correlated observation errors on inverted CO₂ surface fluxes from OCO measurements, *Geophysical Research Letters*, 34, <https://doi.org/10.1029/2007GL030463>, 2007.
- 660 Crippa, M., Guizzardi, D., Muntean, M., Schaaf, E., Vullo, E. L., Solazzo, E., Olivier, J., and Vignati, E.: EDGAR v6.0 Greenhouse Gas Emissions, 2021.
- Crippa, M., Guizzardi, D., Banja, M., Solazzo, E., Muntean, M., Schaaf, E., and Pagani, F.: EDGAR v7 Greenhouse Gas Emissions, 2022.
- 665 Crippa, M., Guizzardi, D., Pagani, F., Schiavina, M., Melchiorri, M., Pisoni, E., Graziosi, F., Muntean, M., Maes, J., Dijkstra, L., Van Damme, M., Clarisse, L., and Coheur, P.: Insights into the spatial distribution of global, national, and subnational greenhouse gas emissions in the Emissions Database for Global Atmospheric Research (EDGAR v8.0), *Earth System Science Data*, 16, 2811–2830, <https://doi.org/10.5194/essd-16-2811-2024>, 2024.
- 670 Davitt, A., Volpato, G., Cheng, X. F., Block, E., Raniga, K., Vandermaal, J., Mendoza, A., McCrary, D., Sutherland, A., Rostami, R., Smith, M., Goodwin, B., Pluard, C., and Schiller, S.: Enteric fermentation and manure management emissions from feedlots and dairies, *WattTime*, Harvard University, Synthetica, Carbon Yield, USA, *Climate TRACE Emissions Inventory*, 2023.
- East, J. D., Jacob, D. J., Balasus, N., Bloom, A. A., Bruhwiler, L., Chen, Z., Kaplan, J. O., Mickley, L. J., Mooring, T. A., Penn, E., Poulter, B., Sulprizio, M. P., Worden, J. R., Yantosca, R. M., and Zhang, Z.: Interpreting the Seasonality of Atmospheric Methane, *Geophysical Research Letters*, 51, e2024GL108494, <https://doi.org/10.1029/2024GL108494>, 2024.
- 675 EIA: *International Energy Statistics*, 2023.
- Etiopie, G., Ciotoli, G., Schwietzke, S., and Schoell, M.: Gridded maps of geological methane emissions and their isotopic signature, *Earth System Science Data*, 11, 1–22, <https://doi.org/10.5194/essd-11-1-2019>, 2019.
- Forni, L., Mautner, M., Lavado, A., Burke, K. F., and Gomez, R. D.: Watershed implications of shale oil and gas production in Vaca Muerta, Argentina, 2021.
- 680 France, J. L., Lunt, M. F., Andrade, M., Moreno, I., Ganesan, A. L., Lachlan-Cope, T., Fisher, R. E., Lowry, D., Parker, R. J., Nisbet, E. G., and Jones, A. E.: Very large fluxes of methane measured above Bolivian seasonal wetlands, *Proceedings of the National Academy of Sciences*, 119, e2206345119, <https://doi.org/10.1073/pnas.2206345119>, 2022.
- 685 Fung, I., John, J., Lerner, J., Matthews, E., Prather, M., Steele, L. P., and Fraser, P. J.: Three-dimensional model synthesis of the global methane cycle, *Journal of Geophysical Research: Atmospheres*, 96, 13033–13065, <https://doi.org/10.1029/91JD01247>, 1991.

- 690 Gloor, M., Gatti, L. V., Wilson, C., Parker, R. J., Boesch, H., Popa, E., Chipperfield, M. P., Poulter, B., Zhang, Z., Basso, L., Miller, J., McNorton, J., Jimenez, C., and Prigent, C.: Large Methane Emissions From the Pantanal During Rising Water-Levels Revealed by Regularly Measured Lower Troposphere CH₄ Profiles, *Global Biogeochemical Cycles*, 35, e2021GB006964, <https://doi.org/10.1029/2021GB006964>, 2021.
- Hasekamp, O., Lorente, A., Hu, H., Butz, A., de Brugh, J., and Landgraf, J.: Algorithm theoretical baseline document for Sentinel-5 Precursor methane retrieval, *Netherlands Institute for Space Research*, 67, 2023.
- 695 Heald, C. L., Jacob, D. J., Jones, D. B. A., Palmer, P. I., Logan, J. A., Streets, D. G., Sachse, G. W., Gille, J. C., Hoffman, R. N., and Nehrkorn, T.: Comparative inverse analysis of satellite (MOPITT) and aircraft (TRACE-P) observations to estimate Asian sources of carbon monoxide, *Journal of Geophysical Research: Atmospheres*, 109, <https://doi.org/10.1029/2004JD005185>, 2004.
- 700 Hmiel, B., Petrenko, V. V., Dyonisius, M. N., Buizert, C., Smith, A. M., Place, P. F., Harth, C., Beaudette, R., Hua, Q., Yang, B., Vimont, I., Michel, S. E., Severinghaus, J. P., Etheridge, D., Bromley, T., Schmitt, J., Faïn, X., Weiss, R. F., and Dlugokencky, E.: Preindustrial 14CH₄ indicates greater anthropogenic fossil CH₄ emissions, *Nature*, 578, 409–412, <https://doi.org/10.1038/s41586-020-1991-8>, 2020.
- IPCC: 2019 Refinement to the 2006 IPCC Guidelines for National Greenhouse Gas Inventories, 2019.
- 705 Jacob, D. J., Varon, D. J., Cusworth, D. H., Dennison, P. E., Frankenberg, C., Gautam, R., Guanter, L., Kelley, J., McKeever, J., Ott, L. E., Poulter, B., Qu, Z., Thorpe, A. K., Worden, J. R., and Duren, R. M.: Quantifying methane emissions from the global scale down to point sources using satellite observations of atmospheric methane, *Atmospheric Chemistry and Physics*, 22, 9617–9646, <https://doi.org/10.5194/acp-22-9617-2022>, 2022.
- 710 Janardanan, R., Maksyutov, S., Tsuruta, A., Wang, F., Tiwari, Y. K., Valsala, V., Ito, A., Yoshida, Y., Kaiser, J. W., Janssens-Maenhout, G., Arshinov, M., Sasakawa, M., Tohjima, Y., Worthy, D. E. J., Dlugokencky, E. J., Ramonet, M., Arduini, J., Lavric, J. V., Piacentino, S., Krummel, P. B., Langenfelds, R. L., Mammarella, I., and Matsunaga, T.: Country-Scale Analysis of Methane Emissions with a High-Resolution Inverse Model Using GOSAT and Surface Observations, *Remote Sensing*, 12, 375, <https://doi.org/10.3390/rs12030375>, 2020.
- Liang, R., Zhang, Y., Chen, W., Zhang, P., Liu, J., Chen, C., Mao, H., Shen, G., Qu, Z., Chen, Z., Zhou, M., Wang, P., Parker, R. J., Boesch, H., Lorente, A., Maasackers, J. D., and Aben, I.: East Asian methane emissions inferred from high-resolution inversions of GOSAT and TROPOMI observations: a comparative and evaluative analysis, *Atmospheric Chemistry and Physics*, 23, 8039–8057, <https://doi.org/10.5194/acp-23-8039-2023>, 2023.
- 715 Lorente, A., Borsdorff, T., Martinez-Velarte, M. C., and Landgraf, J.: Accounting for surface reflectance spectral features in TROPOMI methane retrievals, *Atmospheric Measurement Techniques*, 16, 1597–1608, <https://doi.org/10.5194/amt-16-1597-2023>, 2023.
- 720 Lu, X., Jacob, D. J., Zhang, Y., Maasackers, J. D., Sulprizio, M. P., Shen, L., Qu, Z., Scarpelli, T. R., Nesser, H., Yantosca, R. M., Sheng, J., Andrews, A., Parker, R. J., Boesch, H., Bloom, A. A., and Ma, S.: Global methane budget and trend, 2010–2017: complementarity of inverse analyses using in situ (GLOBALVIEWplus CH₄ ObsPack) and satellite (GOSAT) observations, *Atmospheric Chemistry and Physics*, 21, 4637–4657, <https://doi.org/10.5194/acp-21-4637-2021>, 2021.

- 725 Ma, S., Worden, J. R., Bloom, A. A., Zhang, Y., Poulter, B., Cusworth, D. H., Yin, Y., Pandey, S., Maasackers, J. D., Lu, X., Shen, L., Sheng, J., Frankenberg, C., Miller, C. E., and Jacob, D. J.: Satellite Constraints on the Latitudinal Distribution and Temperature Sensitivity of Wetland Methane Emissions, *AGU Advances*, 2, e2021AV000408, <https://doi.org/10.1029/2021AV000408>, 2021.
- 730 Maasackers, J. D., Jacob, D. J., Sulprizio, M. P., Scarpelli, T. R., Nesser, H., Sheng, J.-X., Zhang, Y., Hersher, M., Bloom, A. A., Bowman, K. W., Worden, J. R., Janssens-Maenhout, G., and Parker, R. J.: Global distribution of methane emissions, emission trends, and OH concentrations and trends inferred from an inversion of GOSAT satellite data for 2010–2015, *Atmospheric Chemistry and Physics*, 19, 7859–7881, <https://doi.org/10.5194/acp-19-7859-2019>, 2019.
- 735 Maasackers, J. D., Jacob, D. J., Sulprizio, M. P., Scarpelli, T. R., Nesser, H., Sheng, J., Zhang, Y., Lu, X., Bloom, A. A., Bowman, K. W., Worden, J. R., and Parker, R. J.: 2010–2015 North American methane emissions, sectoral contributions, and trends: a high-resolution inversion of GOSAT observations of atmospheric methane, *Atmospheric Chemistry and Physics*, 21, 4339–4356, <https://doi.org/10.5194/acp-21-4339-2021>, 2021.
- 740 Maasackers, J. D., Varon, D. J., Elfarsdóttir, A., McKeever, J., Jarvis, D., Mahapatra, G., Pandey, S., Lorente, A., Borsdorff, T., Foorhuis, L. R., Schuit, B. J., Tol, P., van Kempen, T. A., van Hees, R., and Aben, I.: Using satellites to uncover large methane emissions from landfills, *Science Advances*, 8, eabn9683, <https://doi.org/10.1126/sciadv.abn9683>, 2022.
- 740 Marani, L. and Alvalá, P. C.: Methane emissions from lakes and floodplains in Pantanal, Brazil, *Atmospheric Environment*, 41, 1627–1633, <https://doi.org/10.1016/j.atmosenv.2006.10.046>, 2007.
- Murguia-Flores, F., Arndt, S., Ganesan, A. L., Murray-Tortarolo, G., and Hornibrook, E. R. C.: Soil Methanotrophy Model (MeMo v1.0): a process-based model to quantify global uptake of atmospheric methane by soil, *Geoscientific Model Development*, 11, 2009–2032, <https://doi.org/10.5194/gmd-11-2009-2018>, 2018.
- 745 Nathan, B., Maasackers, J. D., Naus, S., Gautam, R., Omara, M., Varon, D. J., Sulprizio, M. P., Lorente, A., Borsdorff, T., Parker, R. J., and Aben, I.: Assessing methane emissions from collapsing Venezuelan oil production using TROPOMI, *EGUsphere*, 1–27, <https://doi.org/10.5194/egusphere-2023-2887>, 2023.
- 750 Nesser, H., Jacob, D. J., Maasackers, J. D., Lorente, A., Chen, Z., Lu, X., Shen, L., Qu, Z., Sulprizio, M. P., Winter, M., Ma, S., Bloom, A. A., Worden, J. R., Stavins, R. N., and Randles, C. A.: High-resolution US methane emissions inferred from an inversion of 2019 TROPOMI satellite data: contributions from individual states, urban areas, and landfills, *Atmospheric Chemistry and Physics*, 24, 5069–5091, <https://doi.org/10.5194/acp-24-5069-2024>, 2024.
- OGCI: Oil & Gas Climate Initiative Reporting Framework (Version 3.6), OGCI, 2022.
- 755 Olson, D. M., Dinerstein, E., Wikramanayake, E. D., Burgess, N. D., Powell, G. V., Underwood, E. C., D'amico, J. A., Itoua, I., Strand, H. E., Morrison, J. C., and others: Terrestrial Ecoregions of the World: A New Map of Life on Earth: A new global map of terrestrial ecoregions provides an innovative tool for conserving biodiversity, *BioScience*, 51, 933–938, 2001.

- 760 Pangala, S. R., Enrich-Prast, A., Basso, L. S., Peixoto, R. B., Bastviken, D., Hornibrook, E. R. C., Gatti, L. V., Marotta, H., Calazans, L. S. B., Sakuragui, C. M., Bastos, W. R., Malm, O., Gloor, E., Miller, J. B., and Gauci, V.: Large emissions from floodplain trees close the Amazon methane budget, *Nature*, 552, 230–234, <https://doi.org/10.1038/nature24639>, 2017.
- Parker, R. and Boesch, H.: University of Leicester GOSAT Proxy XCH4 v9.0, <https://doi.org/10.5285/18EF8247F52A4CB6A14013F8235CC1EB>, 2020.
- 765 Parker, R., Boesch, H., Cogan, A., Fraser, A., Feng, L., Palmer, P. I., Messerschmidt, J., Deutscher, N., Griffith, D. W. T., Notholt, J., Wennberg, P. O., and Wunch, D.: Methane observations from the Greenhouse Gases Observing SATellite: Comparison to ground-based TCCON data and model calculations, *Geophysical Research Letters*, 38, 2011GL047871, <https://doi.org/10.1029/2011GL047871>, 2011.
- 770 Parker, R. J., Webb, A., Boesch, H., Somkuti, P., Barrio Guillo, R., Di Noia, A., Kalaitzi, N., Anand, J. S., Bergamaschi, P., Chevallier, F., Palmer, P. I., Feng, L., Deutscher, N. M., Feist, D. G., Griffith, D. W. T., Hase, F., Kivi, R., Morino, I., Notholt, J., Oh, Y.-S., Ohyama, H., Petri, C., Pollard, D. F., Roehl, C., Sha, M. K., Shiomi, K., Strong, K., Sussmann, R., Té, Y., Velazco, V. A., Warneke, T., Wennberg, P. O., and Wunch, D.: A decade of GOSAT Proxy satellite CH₄ observations, *Earth System Science Data*, 12, 3383–3412, <https://doi.org/10.5194/essd-12-3383-2020>, 2020a.
- 775 Parker, R. J., Wilson, C., Bloom, A. A., Comyn-Platt, E., Hayman, G., McNorton, J., Boesch, H., and Chipperfield, M. P.: Exploring constraints on a wetland methane emission ensemble (WetCHARTs) using GOSAT observations, *Biogeosciences*, 17, 5669–5691, <https://doi.org/10.5194/bg-17-5669-2020>, 2020b.
- Planet Team: Planet imagery product specifications, Planet Team: San Francisco, CA, USA, 2021, 2021.
- 780 Puliafito, S. E., Bolaño-Ortiz, T., Berná, L., and Pascual Flores, R.: High resolution inventory of atmospheric emissions from livestock production, agriculture, and biomass burning sectors of Argentina, *Atmospheric Environment*, 223, 117248, <https://doi.org/10.1016/j.atmosenv.2019.117248>, 2020.
- Qu, Z., Jacob, D. J., Shen, L., Lu, X., Zhang, Y., Scarpelli, T. R., Nesser, H., Sulprizio, M. P., Maasakkers, J. D., Bloom, A. A., Worden, J. R., Parker, R. J., and Delgado, A. L.: Global distribution of methane emissions: a comparative inverse analysis of observations from the TROPOMI and GOSAT satellite instruments, *Atmospheric Chemistry and Physics*, 21, 14159–14175, <https://doi.org/10.5194/acp-21-14159-2021>, 2021.
- 785 Qu, Z., Jacob, D. J., Bloom, A., Worden, J., Parker, R. J., and Boesch, H.: Inverse modeling of satellite observations shows that the wet tropics drive the 2010-2022 methane increase, 2024.
- Randerson, J. T., Chen, Y., van der Werf, G. R., Rogers, B. M., and Morton, D. C.: Global burned area and biomass burning emissions from small fires, *Journal of Geophysical Research: Biogeosciences*, 117, <https://doi.org/10.1029/2012JG002128>, 2012.
- 790 Ringeval, B., Houweling, S., van Bodegom, P. M., Spahni, R., van Beek, R., Joos, F., and Röckmann, T.: Methane emissions from floodplains in the Amazon Basin: challenges in developing a process-based model for global applications, *Biogeosciences*, 11, 1519–1558, <https://doi.org/10.5194/bg-11-1519-2014>, 2014.

Rodgers, C. D.: Inverse Methods for Atmospheric Sounding, WORLD SCIENTIFIC, 256 pp.,
<https://doi.org/10.1142/3171>, 2000.

- 795 Saunio, M., Stavert, A. R., Poulter, B., Bousquet, P., Canadell, J. G., Jackson, R. B., Raymond, P. A.,
Dlugokencky, E. J., Houweling, S., Patra, P. K., Ciais, P., Arora, V. K., Bastviken, D., Bergamaschi, P., Blake, D.
R., Brailsford, G., Bruhwiler, L., Carlson, K. M., Carrol, M., Castaldi, S., Chandra, N., Crevoisier, C., Crill, P.
M., Covey, K., Curry, C. L., Etiope, G., Frankenberg, C., Gedney, N., Hegglin, M. I., Höglund-Isaksson, L.,
Hugelius, G., Ishizawa, M., Ito, A., Janssens-Maenhout, G., Jensen, K. M., Joos, F., Kleinen, T., Krummel, P. B.,
800 Langenfelds, R. L., Laruelle, G. G., Liu, L., Machida, T., Maksyutov, S., McDonald, K. C., McNorton, J., Miller,
P. A., Melton, J. R., Morino, I., Müller, J., Murguia-Flores, F., Naik, V., Niwa, Y., Noce, S., O'Doherty, S., Parker,
R. J., Peng, C., Peng, S., Peters, G. P., Prigent, C., Prinn, R., Ramonet, M., Regnier, P., Riley, W. J., Rosentreter,
J. A., Segers, A., Simpson, I. J., Shi, H., Smith, S. J., Steele, L. P., Thornton, B. F., Tian, H., Tohjima, Y., Tubiello,
F. N., Tsuruta, A., Viovy, N., Voulgarakis, A., Weber, T. S., van Weele, M., van der Werf, G. R., Weiss, R. F.,
805 Worthy, D., Wunch, D., Yin, Y., Yoshida, Y., Zhang, W., Zhang, Z., Zhao, Y., Zheng, B., Zhu, Q., Zhu, Q., and
Zhuang, Q.: The Global Methane Budget 2000–2017, *Earth System Science Data*, 12, 1561–1623,
<https://doi.org/10.5194/essd-12-1561-2020>, 2020.

- Saunio, M., Martinez, A., Poulter, B., Zhang, Z., Raymond, P., Regnier, P., Canadell, J. G., Jackson, R. B., Patra,
P. K., Bousquet, P., Ciais, P., Dlugokencky, E. J., Lan, X., Allen, G. H., Bastviken, D., Beerling, D. J., Belikov, D.
810 A., Blake, D. R., Castaldi, S., Crippa, M., Deemer, B. R., Dennison, F., Etiope, G., Gedney, N., Höglund-
Isaksson, L., Holgerson, M. A., Hopcroft, P. O., Hugelius, G., Ito, A., Jain, A. K., Janardanan, R., Johnson, M. S.,
Kleinen, T., Krummel, P., Lauerwald, R., Li, T., Liu, X., McDonald, K. C., Melton, J. R., Mühle, J., Müller, J.,
Murguia-Flores, F., Niwa, Y., Noce, S., Pan, S., Parker, R. J., Peng, C., Ramonet, M., Riley, W. J., Rocher-Ros,
G., Rosentreter, J. A., Sasakawa, M., Segers, A., Smith, S. J., Stanley, E. H., Thanwerdas, J., Tian, H., Tsuruta, A.,
815 Tubiello, F. N., Weber, T. S., van der Werf, G., Worthy, D. E., Xi, Y., Yoshida, Y., Zhang, W., Zheng, B., Zhu, Q.,
Zhu, Q., and Zhuang, Q.: Global Methane Budget 2000–2020, *Earth System Science Data Discussions*, 1–
147, <https://doi.org/10.5194/essd-2024-115>, 2024.

Scarpelli, T. R. and Jacob, D. J.: Global Fuel Exploitation Inventory (GFEL),
<https://doi.org/10.7910/DVN/HH4EUM>, 2021.

- 820 Scarpelli, T. R., Jacob, D. J., Grossman, S., Lu, X., Qu, Z., Sulprizio, M. P., Zhang, Y., Reuland, F., Gordon, D.,
and Worden, J. R.: Updated Global Fuel Exploitation Inventory (GFEL) for methane emissions from the oil, gas,
and coal sectors: evaluation with inversions of atmospheric methane observations, *Atmospheric Chemistry and
Physics*, 22, 3235–3249, <https://doi.org/10.5194/acp-22-3235-2022>, 2022.

- Shen, L., Zavala-Araiza, D., Gautam, R., Omara, M., Scarpelli, T., Sheng, J., Sulprizio, M. P., Zhuang, J., Zhang,
825 Y., Qu, Z., Lu, X., Hamburg, S. P., and Jacob, D. J.: Unravelling a large methane emission discrepancy in Mexico
using satellite observations, *Remote Sensing of Environment*, 260, 112461,
<https://doi.org/10.1016/j.rse.2021.112461>, 2021.

- Shen, L., Jacob, D. J., Gautam, R., Omara, M., Scarpelli, T. R., Lorente, A., Zavala-Araiza, D., Lu, X., Chen, Z.,
830 and Lin, J.: National quantifications of methane emissions from fuel exploitation using high resolution inversions
of satellite observations, *Nat Commun*, 14, 4948, <https://doi.org/10.1038/s41467-023-40671-6>, 2023.

- Sierra, C., de Araújo, A., and van Asperen, H., Botía, S., Candido, L., Chanca, I., Correa, C. S. C., Eritt, M., Gatti, L., Hammer, S., Heimann, M., Jordan, A., Kneißl, R., Lavric, J. V., Levin, I., Macario, K., Moossen, H., Quesada, C. A., Rödenbeck, C., Santos, Y., Steinhof, A., Takeshi, B., Trumbore, S., Zaehle, S.: Greenhouse gases, isotopes ratios and related gases measured at the ATTO station, 2024.
- 835 Szopa, S., Naik, V., Adhikary, B., Artaxo, P., Berntsen, T., Collins, W., Fuzzi, S., Gallardo, L., Kiendler-Scharr, A., Klimont, Z., and others: Short-lived climate forcers Climate Change 2021: The Physical Science Basis. Contribution of Working Group I to the Sixth Assessment Report of the Intergovernmental Panel on Climate Change ed V Masson-Delmotte et al, 2021.
- 840 Tunnicliffe, R. L., Ganesan, A. L., Parker, R. J., Boesch, H., Gedney, N., Poulter, B., Zhang, Z., Lavrič, J. V., Walter, D., Rigby, M., Henne, S., Young, D., and O'Doherty, S.: Quantifying sources of Brazil's CH₄ emissions between 2010 and 2018 from satellite data, *Atmospheric Chemistry and Physics*, 20, 13041–13067, <https://doi.org/10.5194/acp-20-13041-2020>, 2020.
- Turner, A. J. and Jacob, D. J.: Balancing aggregation and smoothing errors in inverse models, *Atmospheric Chemistry and Physics*, 15, 7039–7048, <https://doi.org/10.5194/acp-15-7039-2015>, 2015.
- 845 Varon, D. J., Jacob, D. J., Sulprizio, M., Estrada, L. A., Downs, W. B., Shen, L., Hancock, S. E., Nesser, H., Qu, Z., Penn, E., Chen, Z., Lu, X., Lorente, A., Tewari, A., and Randles, C. A.: Integrated Methane Inversion (IMI 1.0): a user-friendly, cloud-based facility for inferring high-resolution methane emissions from TROPOMI satellite observations, *Geoscientific Model Development*, 15, 5787–5805, <https://doi.org/10.5194/gmd-15-5787-2022>, 2022.
- 850 Veefkind, J. P., Aben, I., McMullan, K., Förster, H., de Vries, J., Otter, G., Claas, J., Eskes, H. J., de Haan, J. F., Kleipool, Q., van Weele, M., Hasekamp, O., Hoogeveen, R., Landgraf, J., Snel, R., Tol, P., Ingmann, P., Voors, R., Kruizinga, B., Vink, R., Visser, H., and Levelt, P. F.: TROPOMI on the ESA Sentinel-5 Precursor: A GMES mission for global observations of the atmospheric composition for climate, air quality and ozone layer applications, *Remote Sensing of Environment*, 120, 70–83, <https://doi.org/10.1016/j.rse.2011.09.027>, 2012.
- 855 Wecht, K. J., Jacob, D. J., Frankenberg, C., Jiang, Z., and Blake, D. R.: Mapping of North American methane emissions with high spatial resolution by inversion of SCIAMACHY satellite data, *Journal of Geophysical Research: Atmospheres*, 119, 7741–7756, <https://doi.org/10.1002/2014JD021551>, 2014.
- 860 van der Werf, G. R., Randerson, J. T., Giglio, L., van Leeuwen, T. T., Chen, Y., Rogers, B. M., Mu, M., van Marle, M. J. E., Morton, D. C., Collatz, G. J., Yokelson, R. J., and Kasibhatla, P. S.: Global fire emissions estimates during 1997–2016, *Earth System Science Data*, 9, 697–720, <https://doi.org/10.5194/essd-9-697-2017>, 2017.
- Wilson, C., Gloor, M., Gatti, L. V., Miller, J. B., Monks, S. A., McNorton, J., Bloom, A. A., Basso, L. S., and Chipperfield, M. P.: Contribution of regional sources to atmospheric methane over the Amazon Basin in 2010 and 2011, *Global Biogeochemical Cycles*, 30, 400–420, <https://doi.org/10.1002/2015GB005300>, 2016.
- 865 Wilson, C., Chipperfield, M. P., Gloor, M., Parker, R. J., Boesch, H., McNorton, J., Gatti, L. V., Miller, J. B., Basso, L. S., and Monks, S. A.: Large and increasing methane emissions from eastern Amazonia derived from

satellite data, 2010–2018, *Atmospheric Chemistry and Physics*, 21, 10643–10669, <https://doi.org/10.5194/acp-21-10643-2021>, 2021.

870 Worden, J. R., Cusworth, D. H., Qu, Z., Yin, Y., Zhang, Y., Bloom, A. A., Ma, S., Byrne, B. K., Scarpelli, T.,
Maasackers, J. D., Crisp, D., Duren, R., and Jacob, D. J.: The 2019 methane budget and uncertainties at 1°
resolution and each country through Bayesian integration Of GOSAT total column methane data and a priori
inventory estimates, *Atmospheric Chemistry and Physics*, 22, 6811–6841, <https://doi.org/10.5194/acp-22-6811-2022>, 2022.

875 Yu, X., Millet, D. B., Henze, D. K., Turner, A. J., Delgado, A. L., Bloom, A. A., and Sheng, J.: A high-resolution
satellite-based map of global methane emissions reveals missing wetland, fossil fuel and monsoon sources,
Gases/Atmospheric Modelling/Troposphere/Chemistry (chemical composition and reactions),
<https://doi.org/10.5194/egusphere-2022-948>, 2022.

880 Zhang, B., Tian, H., Lu, C., Chen, G., Pan, S., Anderson, C., and Poulter, B.: Methane emissions from global
wetlands: An assessment of the uncertainty associated with various wetland extent data sets, *Atmospheric
Environment*, 165, 310–321, <https://doi.org/10.1016/j.atmosenv.2017.07.001>, 2017.

Zhang, Y., Jacob, D. J., Lu, X., Maasackers, J. D., Scarpelli, T. R., Sheng, J.-X., Shen, L., Qu, Z., Sulprizio, M. P.,
Chang, J., Bloom, A. A., Ma, S., Worden, J., Parker, R. J., and Boesch, H.: Attribution of the accelerating increase
in atmospheric methane during 2010–2018 by inverse analysis of GOSAT observations, *Atmospheric Chemistry
and Physics*, 21, 3643–3666, <https://doi.org/10.5194/acp-21-3643-2021>, 2021.

885 Zhang, Z., Zimmermann, N. E., Kaplan, J. O., and Poulter, B.: Modeling spatiotemporal dynamics of global
wetlands: comprehensive evaluation of a new sub-grid TOPMODEL parameterization and uncertainties,
Biogeosciences, 13, 1387–1408, <https://doi.org/10.5194/bg-13-1387-2016>, 2016.

890 Zhang, Z., Zimmermann, N. E., Calle, L., Hurtt, G., Chatterjee, A., and Poulter, B.: Enhanced response of global
wetland methane emissions to the 2015–2016 El Niño-Southern Oscillation event, *Environ. Res. Lett.*, 13,
074009, <https://doi.org/10.1088/1748-9326/aac939>, 2018.

Ziegler-Rodriguez, K., Margallo, M., Aldaco, R., Vázquez-Rowe, I., and Kahhat, R.: Transitioning from open
dumpsters to landfilling in Peru: Environmental benefits and challenges from a life-cycle perspective, *Journal of
Cleaner Production*, 229, 989–1003, <https://doi.org/10.1016/j.jclepro.2019.05.015>, 2019.